Article

Self-aligned optical microcomb emerging between octave-separated lasers

https://doi.org/10.1038/s41586-026-11086-2

Received: 4 February 2026

Accepted: 26 August 2026

Published online: 30 September 2026

Check for updates

Grégory Moille[1,2]✉, Pradyoth Shandilya[3], Jordan Stone[2], River Beard[4], Shao-Chien Ou[1,2], Zongda Li[5,6], Mark Harrington[7], Kaikai Liu[7], Robert Rockmore[8], Curtis R. Menyuk[3], Daniel J. Blumenthal[7], Sean P. Krzyzewski[8], Miro Erkintalo[5,6] & Kartik Srinivasan[1,2]✉

Optical frequency combs (OFCs) are frequency rulers essential for precision metrology, next-generation navigation and testing of fundamental physics[1]. Despite intense efforts, chip-integrated OFCs remain laboratory-bound, unable to fulfil their promise of compact and cost-effective deployment. Although improvements in fabrication and integration are important, a conceptual limitation has stymied progress: on-chip OFC architectures have aimed to miniaturize their table-top counterparts and relied on cascading outward from a single pump[2,3]. In integrated platforms, this approach does not readily generate the strong, low-noise, octave-spaced signals crucial for robust zero-frequency offset detection[4]. Here we overcome this limitation through an architectural inversion, in which an optical microcomb fills the spectrum between two octave-separated pumps. The two pumps generate a parametrically driven cavity soliton[5] in an integrated $\chi^{(3)}$ resonator[6], which robustly self-aligns to both pumps across multiple foundry-fabricated devices and operating configurations. This produces a single octave-spanning comb from telecom to visible wavelengths, whose zero-frequency offset is defined by the harmonic offset of the pumps and can therefore be reliably detected and stabilized. We showcase the capabilities of our platform by executing all of the three core tasks of OFC metrology: optical frequency synthesis, low-noise millimetre-wave generation and integrated optical clock readout, using the same self-aligned microcomb with only its input locks changed.

Ultrahigh-precision optical frequency measurement and stabilization enables positioning, navigation and timing beyond Global Positioning System (GPS)[7], quantum computing[8], quantum sensing[9] and fundamental physics measurements[10], and may redefine the second[11]. Optical frequency combs (OFCs)—optical frequency rulers with evenly spaced markers and a known zero-frequency offset[1]—are a key enabling technology for these applications, providing a coherent optical-to-microwave two-way link for ultrahigh-precision optical frequency measurement[12], synthesis[13] and ultralow noise microwave generation[14]. Reducing the size, weight, power and cost (SWaP-C) of OFCs through mass-scale fabrication can enable field deployment and the lab-to-consumer transition along with the critical technologies they empower. This vision has driven efforts to generate OFCs in integrated photonics platforms.

Miniaturizing from the table top to the chip scale, integrated OFCs rely on using the second-order ($\chi^{(2)}$) or third-order ($\chi^{(3)}$) optical nonlinearity to spectrally broaden a narrow-band input to obtain evenly spaced comb teeth spanning an octave[15–18], thus enabling ν–2ν (also referred to as f–2f) nonlinear interferometry to measure and stabilize the carrier-envelope offset (CEO) of the comb[19,20]. Dissipative Kerr solitons (DKSs) in on-chip microresonators[2] constitute a particular system of interest that leverages the $\chi^{(3)}$ nonlinearity of the photonic material as an ultra-broadband gain medium. Generated from a continuous-wave pump laser, chip-integrated DKS combs can span an octave[3] and are compatible with mass-scale foundry fabrication[21,22] and low power consumption[23]. Although DKS combs have proven their effectiveness in numerous applications[1,2,24], their outward cascading from a low-power seed pump laser leads to fundamental metrology limitations. Octave-spaced signals at the comb edges are typically very weak and noisy (due to thermo-refractive fluctuations[4]), which greatly hinders the detection and stabilization of the CEO. These limitations have restricted precise predictability of the DKS repetition rate[25], and direct CEO detection and locking, to a small handful of laboratory demonstrations[4,26–31] that involve complex apparatuses and/or additional helper lasers, limiting deployable integrated frequency metrology.

In this work, we demonstrate a new paradigm for integrated OFC generation and self-referencing. Fundamentally departing from conventional comb generation architectures that rely on cascading outwards from a single pump, our concept is underpinned by recently discovered parametrically driven cavity solitons (PDCSs)[5] that can manifest themselves in $\chi^{(3)}$ resonators driven by two continuous-wave pump lasers[6], corresponding to frequency combs that are centred in between the two pumps. Here, we report on two transformative advances in integrated $\chi^{(3)}$ PDCS generation that underline their direct

[1]Joint Quantum Institute, NIST/University of Maryland, College Park, MD, USA. [2]Microsystems and Nanotechnology Division, National Institute of Standards and Technology, Gaithersburg, MD, USA. [3]University of Maryland Baltimore County, Baltimore, MD, USA. [4]AV Incorporated, Albuquerque, NM, USA. [5]Department of Physics, University of Auckland, Auckland, New Zealand. [6]The Dodd-Walls Centre for Photonic and Quantum Technologies, Dunedin, New Zealand. [7]Department of Electrical and Computer Engineering, University of California Santa Barbara, Santa Barbara, CA, USA. [8]Air Force Research Laboratory, Space Vehicles Directorate, Kirtland Air Force Base, Albuquerque, NM, USA. ✉e-mail: gmoille@umd.edu; kartik.srinivasan@nist.gov

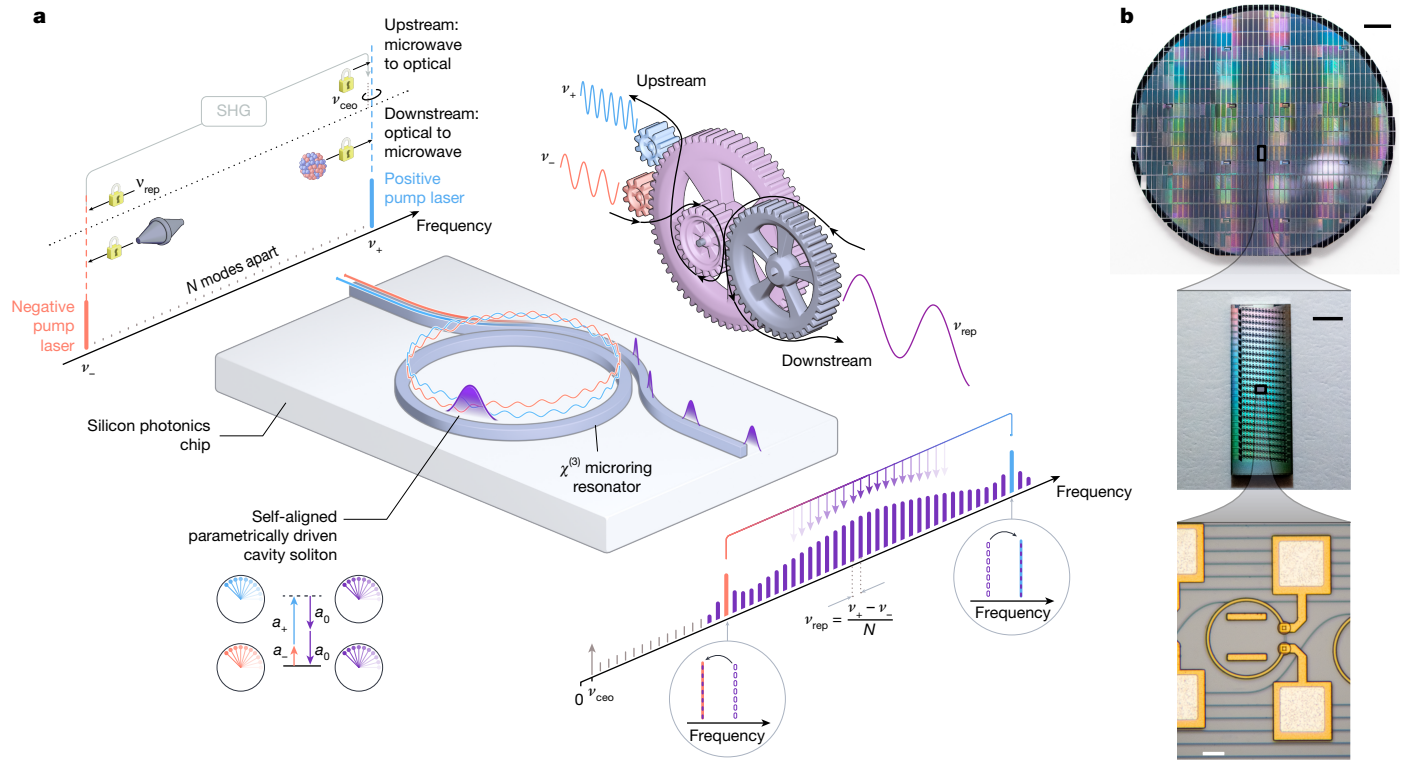


Fig. 1 | Concept of self-aligned PDCS microcomb generation with octave-separated lasers. a, Schematic of dual-pump PDCS generation. Two pump lasers (with frequencies ν_- and $\nu_+ \approx 2\nu_-$) are injected into a $\chi^{(3)}$ microring resonator, in which they interact nonlinearly to generate a PDCS. By minimizing their phase difference, the Kerr nonlinearity phase-locks all components (lower left inset), leading to the PDCS self-synchronizing to both the pump fields. The output microcomb spectrally fills the gap between the two pump lasers, with both capturing their nearest PDCS comb teeth to form a unique, single frequency grid. The repetition rate thus becomes deterministic as $\nu_{rep}^{pdcs} = (\nu_+ - \nu_-)/N$, where ν_+, ν_- and N are all known. Moreover, the quasi-harmonic pump configuration enables CEO definition (ν_{ceo}) and locking before comb generation, for complete system self-stabilization, which in turn enables straightforward interfacing with locked lasers and microwave sources for core OFC tasks in both the microwave and optical domains. SHG, second harmonic generation. **b**, Photographs (top and centre) and micrograph (bottom) of the 100-mm foundry-fabricated silicon nitride wafer (Methods), in which our new deployable microcomb architecture is demonstrated. Scale bars, 1 cm (**b**, top); 1 mm (**b**, middle); 10 μm (**b**, bottom).

potential for comb metrology: (1) the ability to generate on-chip PDCS combs with two octave-separated pumps; and (2) the possibility that a generated PDCS comb can nonlinearly align itself with the pumps, resulting in a single frequency grid across the entire pump span. These advances are robust across multiple foundry-fabricated devices and pump configurations, and produce a single octave-spanning OFC from telecom to visible wavelengths with intrinsic two-point microcomb stabilization control. Because the octave-separated pumps are both comb lines (when operating in the self-alignment regime), the CEO of the subsequently generated PDCS is determined a priori before the chip from the harmonic offset between the pumps, enabling flexible interfacing with microwave and optical frequency references. We show that by simply changing how the input lasers are locked, the same self-aligned PDCS can perform the three core tasks of self-referenced OFCs: synthesizing optical frequencies from known microwave frequencies, generating low-noise micro- or millimetre-waves from low-noise lasers and generating a stable microwave timing signal from an atomically referenced laser.

Concept and experimental demonstration

Unlike a conventional DKS driven by one pump, our concept uses two pumps at frequencies $\nu_\pm$ and azimuthal modes $n_\pm$ (Fig. 1a) driving a chip-integrated $\chi^{(3)}$ microring cavity. When the degenerate four-wave mixing, $\nu_+ + \nu_- = 2\nu_0$, is phase- and frequency-matched, and the light at ν_0 experiences anomalous dispersion, the resonator sustains a broadband PDCS around ν_0 (ref. 6).

Inside the resonator, the PDCS nonlinearly interacts with the fields at the pump frequencies $\nu_\pm$ to produce frequency combs around those pumps. The Kerr nonlinearity locks the group velocities of the PDCS and pump combs, yielding identical repetition rates (comb line spacings). However, the fields at $\nu_\pm$ and ν_0 generally have different phase velocities, giving the combs different CEO frequencies[32]. The output, therefore, consists of three frequency grids: the central PDCS and one around each pump. All share ν_{rep}, but the ν_- and ν_+ grids are offset from the PDCS by $-\Delta\nu_{ceo}$ and $+\Delta\nu_{ceo}$, respectively.

The metrological uses of PDCS combs may seem limited because they do not generally form a single frequency grid, instead exhibiting a new degree of freedom, $\Delta\nu_{ceo}$. Linear theory asserts that the frequency offset $\Delta\nu_{ceo}$ is determined by the resonator dispersion and the detunings of the pump lasers[6]. Although $\Delta\nu_{ceo} = 0$ would be theoretically possible, reaching and maintaining it could be expected to require judicious dispersion engineering and pump-detuning stabilization. However, simulations show that this expectation is inaccurate at small $\Delta\nu_{ceo}$. Instead, Kerr nonlinearity self-aligns the PDCS to the pumps, locking $\Delta\nu_{ceo} = 0$ over a broad parameter range, including pump frequencies (Fig. 1a and Supplementary Information section 1). Although this self-alignment is conceptually related to Kerr-induced synchronization (KIS)[33], in which a single DKS comb tooth is captured by a weak externally injected reference laser, the two phenomena differ fundamentally. In KIS, the reference weakly perturbs a DKS and has no role in the energy balance of the soliton. By contrast, in the self-alignment regime described here, the two pump fields simultaneously synchronize and generate the PDCS through a fully non-perturbative

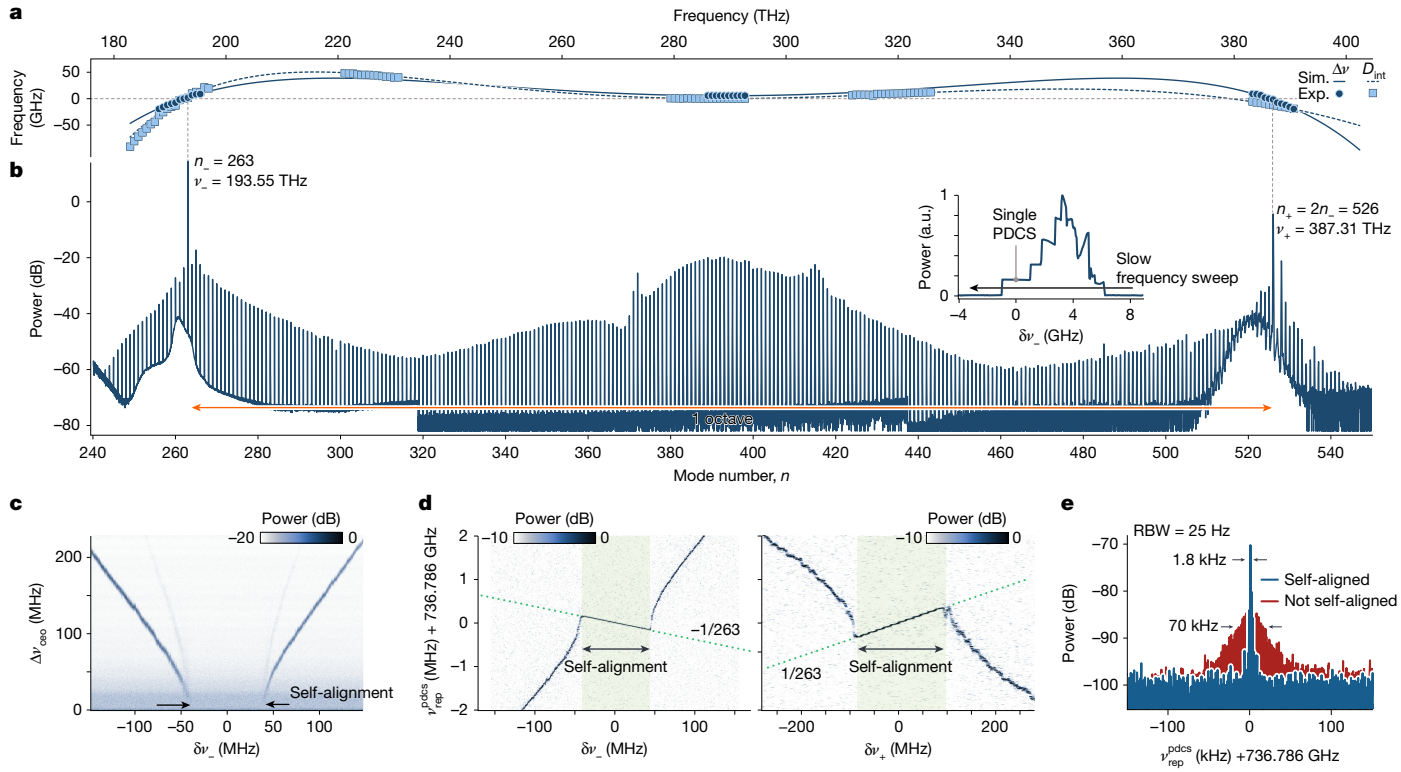


Fig. 2 | Demonstration of self-aligned octave-spanning PDCS microcomb. **a**, Dispersion engineering for dual-pump PDCS generation (RW = 850 nm). OPO frequency mismatch $\Delta\nu$ (circles denote measured values, and the solid line denotes simulation) when pumped at $n_- = 263$ ($\nu_- = 193.55$ THz) and $n_+ = 2n_- = 526$ ($\nu_+ = 387.31$ THz) is minimized at $2n_0 = n_- + n_+ + 1$, enabling PDCS generation. PDCS-integrated dispersion $D_{\mathrm{int}}(n)$ (squares denote measured values, and the dashed line denotes simulation) exhibits zero-crossing at both pumps, minimizing their phase offset with respect to the PDCS to enable efficient self-alignment. **b**, Octave-spanning PDCS spectrum demonstrating a gap-free, 220-THz span single frequency grid with all comb teeth above −60 dB. The power is referenced to 1 mW, that is, equivalent to dBm. Inset, adiabatic PDCS access through slow pump frequency tuning. **c**, Spectrogram from the homodyne detection of the frequency offset $\Delta\nu_{\mathrm{ceo}}$ between the PDCS and ν_+ comb components as a function of negative pump-frequency detuning $\delta\nu_-$. $\Delta\nu_{\mathrm{ceo}}$ is observed to vanish over a finite range, signalling the formation of a single frequency grid because of the self-alignment of the PDCS to the pumps. **d**, Repetition rate disciplining: once self-aligned, $\nu_{\mathrm{rep}}^{\mathrm{pdcs}}$ directly follows the optical frequency division set by the pump separation ($N = 263$) and is linearly disciplined against the pump-frequency detuning. **e**, Therefore, the self-alignment substantially reduces the repetition rate noise compared with the three-comb-component PDCS, detailed in the next section. The power is referenced to 1 mW, that is, equivalent to dBm.

interaction, essentially giving rise to a new self-aligned nonlinear state.

The possibility of PDCS self-alignment has substantial ramifications for on-chip metrology applications if the two pumps generating and capturing the PDCS are to be quasi-harmonically related, that is, $\nu_+ \approx 2\nu_-$ and $n_+ = 2n_-$. Because both pumps become part of the PDCS comb, they satisfy $\nu_+ = 2n_-\nu_{\mathrm{rep}}^{\mathrm{pdcs}} + \nu_{\mathrm{ceo}}^{\mathrm{pdcs}}$ and $\nu_- = n_-\nu_{\mathrm{rep}}^{\mathrm{pdcs}} + \nu_{\mathrm{ceo}}^{\mathrm{pdcs}}$. The CEO can therefore be readily measured and stabilized before the chip from the strong beat between one of the pumps at ν_+ and the other doubled pump at $2\nu_-$. Thus, we can choose a standard two-point locking architecture[34–36] with locked lasers or set the CEO frequency for complete self-referencing while keeping another degree of freedom for repetition rate stabilization or optical locking to cavity references or atomic clocks.

We demonstrate this concept experimentally using silicon nitride (Si_3N_4) microring resonators fabricated on commercial 100-mm wafers, with a bus waveguide designed to couple across more than an octave (Fig. 1b and Methods). The microring dimensions are carefully designed to engineer the resonator dispersion (Fig. 2a) for both PDCS existence through phase and frequency matching and self-alignment to octave-separated pump lasers. The first requirement is the degenerate optical parametric oscillation (OPO) condition, minimizing the frequency mismatch $\Delta\nu(n)$ between the pumped resonances and generation resonance at the centre mode n_0 (Methods). The second, for the self-alignment, requires the PDCS integrated dispersion D_{int} to be close to zero at both pumps, minimizing the phase velocity mismatch between the PDCS and its pumps (Methods).

Figure 2 shows octave-spanning, self-aligned PDCS generation. The dispersion conditions are satisfied at $\nu_- \approx 193$ THz ($n_- = 263$, C-band) and $\nu_+ \approx 387$ THz ($n_+ = 2n_- = 526$, visible) (Fig. 2a). In the linear regime, the positive frequency mismatch $\Delta\nu(n_0) > 0$ is sufficiently small that dual-pump thermo-optic effects can achieve $\Delta\nu(n_0) \approx 0$ (Supplementary Information section 3). Using on-chip pump powers of $P_- = 145$ mW and $P_+ = 70$ mW for the pumps at ν_- and ν_+, respectively, we deterministically generate an octave-spanning PDCS (Fig. 2b and Methods). This procedure produces a continuous single-frequency grid, with all comb teeth between the two octave-separated pump lasers above 1 nW (that is, −60 dBm). Together with the wafer-scale fabrication by which the devices are created and latitude on geometric parameters, as shown in Supplementary Information section 6, we find the realization of self-aligned octave-spanning PDCSs to be as simple as conventional octave-spanning DKSs.

We demonstrate self-alignment by directly measuring $\Delta\nu_{\mathrm{ceo}}$ between the PDCS and the ν_+ pump comb (Methods and Supplementary Information section 5). Tuning ν_- actuates $\Delta\nu_{\mathrm{ceo}}$ (Fig. 2c), which vanishes and locks to zero over a finite pump-frequency range. This locking confirms that the PDCS has self-aligned to the pumps as a single octave-spanning comb.

In a self-aligned PDCS, both pumps are comb teeth that pin $\nu_{\mathrm{rep}}^{\mathrm{pdcs}} = (\nu_+ - \nu_-)/(n_+ - n_-)$. The repetition rate therefore depends linearly on the pump detunings $\delta\nu_\pm$, with opposite signs for positive and negative pump actuation and slope magnitude $1/N = 1/(n_+ - n_-) = 1/n_-$ corresponding to the optical frequency division (OFD) factor (Fig. 2d). Owing to

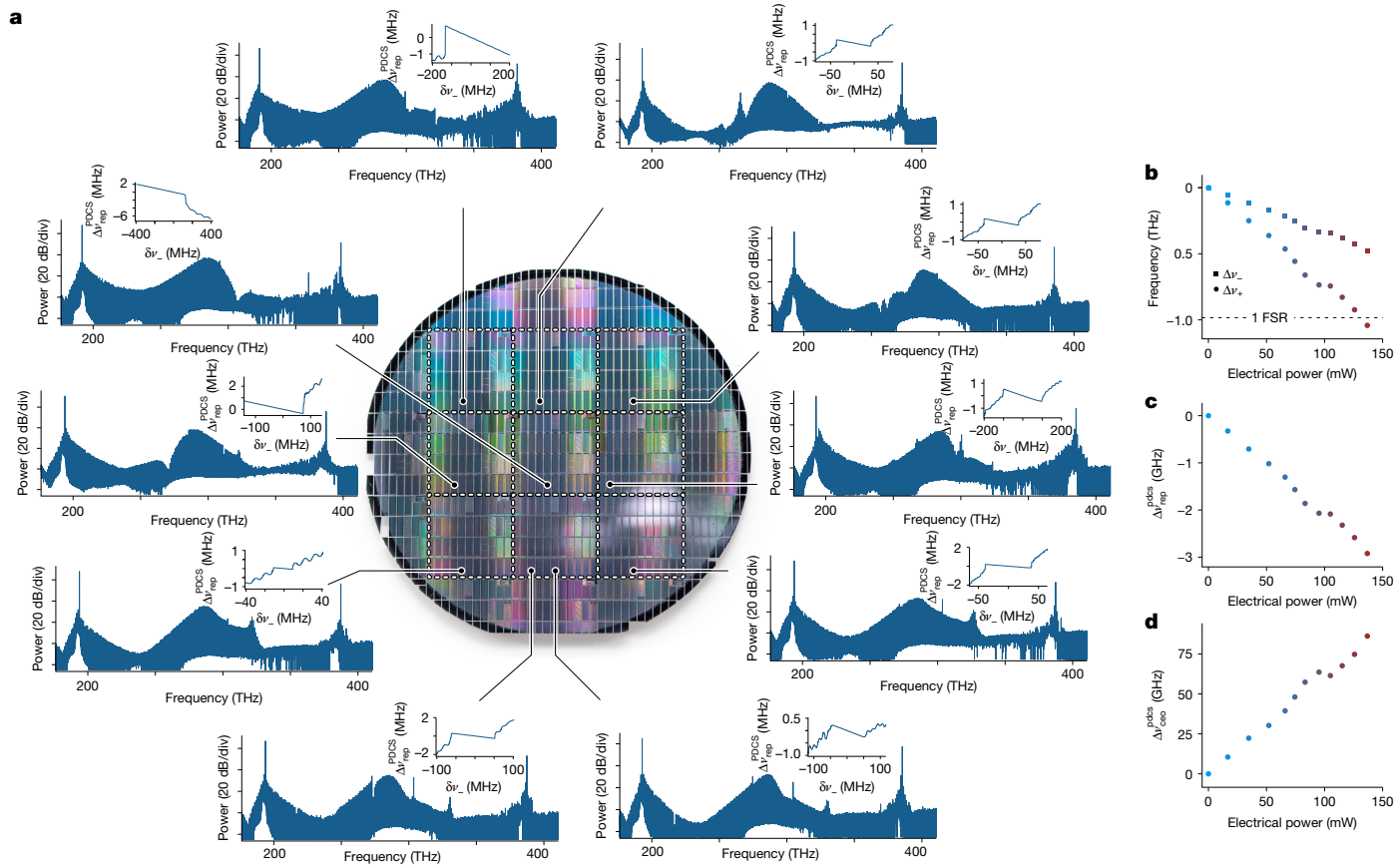


Fig. 3 | Wafer-scale self-aligned PDCS yield and active thermal tuning. **a**, The 100-mm silicon nitride wafer, with dashed rectangles indicating the repeating 22 mm × 22 mm reticle field. For 10 devices sampled across the wafer with purposely different coupler designs, all operated at a quasi-harmonic pump setting enabling CEO detection before the chip, and the corresponding self-aligned PDCS optical spectrum is shown alongside the repetition rate variation against $\delta\nu_-$ (inset), confirming self-alignment and robustness against coupling variations, thickness variations and wafer-scale fabrication imperfections, with the required ν_- adjustment between devices remaining below about 130 GHz, well within the heater thermo-optic tuning range. More examples of successful operation with different devices are provided in the Supplementary Information. **b**–**d**, Active thermal tuning of self-aligned PDCS comb using integrated heaters (Fig. 1b). Joule heating (**b**) enables continuous tuning of the negative (ν_-, squares) and positive (ν_+, circles) pump frequencies required for self-aligned operation, with tuning of ν_+ over one full FSR achieved with 135 mW of electrical power. Thermal tuning (**c**,**d**) also enables tuning of ν_{rep}^{pdcs} and ν_{ceo}^{pdcs}, both of which are fully defined by the pump frequencies. In **b**–**d**, the reference values are $\nu_- = 192.723$ THz, $\nu_+ = 385.275$ THz, $\nu_{rep}^{pdcs} = 997.681$ GHz, and $\nu_{ceo}^{pdcs} = 170.429$ GHz.

self-alignment, the repetition rate noise depends only on the pump-frequency noises, reducing its 3-dB linewidth from 70 kHz for the free-running case with three comb components to 1.8 kHz (Fig. 2e).

Although the conditions required to obtain self-alignment of a PDCS may seem stringent, coupling engineering provides sufficient pump-detuning flexibility to fulfil them across multiple devices and pumped mode pairs (Methods and Supplementary Information section 6). This robustness suits wafer-scale fabrication, in which unavoidable Si_3N_4 film-thickness variations from deposition stress[22] shift dispersion, resonance frequencies and coupling conditions. To demonstrate wafer-scale compatibility, we used another wafer that allows for tests across most of its area. Because of the thicker Si_3N_4 deposition, we use a different nominal geometry than in Fig. 2, yielding a different FSR (Methods). We show that regardless of the position on the 100-mm wafer, the sampled devices all yield quasi-harmonic self-aligned PDCSs (Fig. 3a). Beyond the 10 devices in Fig. 3a, additional chips of the same nominal design from this wafer and other wafers of the same nominal thickness also generate self-aligned PDCSs, confirming reproducibility across wafer positions and between wafers (Supplementary Information section 6). The variations in the optical comb spectra in Fig. 3a reflect the purposely different coupler designs, further demonstrating robustness against coupling variations. Microrings of identical nominal geometry, pumped on the same modes, all produce a self-aligned PDCS, but Si_3N_4 thickness variation slightly shifts the absolute pump frequencies required from device to device. These variations can be compensated by using integrated heaters (Fig. 1b); our measurements show that Joule heating enables tuning of ν_+ by more than one ν_{rep}^{pdcs} with only 135 mW of electrical power (Fig. 3b), along with ν_{ceo}^{pdcs} and ν_{rep}^{pdcs} (Fig. 3c,d), all while preserving the self-aligned state (Supplementary Information section 7). These results establish the foundry compatibility of the platform, for which integrated microcomb CEO detection is now a trivial task.

Self-aligned PDCS metrology

To demonstrate the potential of the self-aligned PDCS OFC, we show its straightforward implementation in metrology applications. As described above, the octave-separated input lasers define a locked CEO frequency that the generated PDCS must possess. Self-stabilization of the OFC becomes equivalent to locking the two pumps to each other (through SHG), while another degree of freedom remains available for optical or repetition rate locking. Thus, rather than a dedicated DKS for a specific application, our integrated self-aligned PDCS operates bidirectionally between the microwave and optical domains, simply by changing the locking point of the input lasers. Although standard for commercial fibre-based frequency combs, this operation has not been readily available in microcombs.

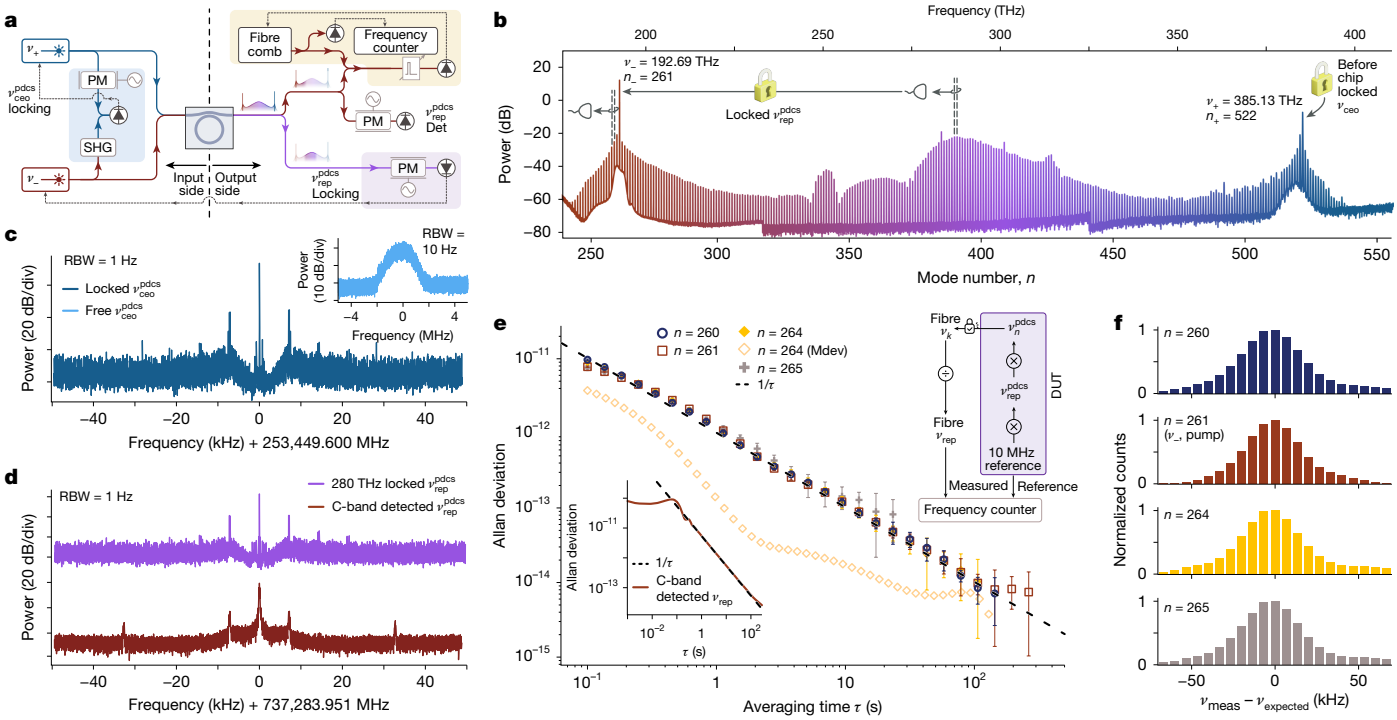


Fig. 4 | Microwave-to-optical link: self-aligned PDCS self-referencing for optical frequency synthesis. a, Simplified experimental setup for optical frequency synthesis using a self-aligned PDCS microcomb. The CEO locking module (blue), entirely before the chip, doubles ν_- and beats it against ν_+, with stabilization achieved by feedback onto ν_+. An EO comb downconverts the CEO beat, which exceeds the direct photodetection bandwidth. The remaining ν_- degree of freedom locks the repetition rate ν_{rep}, detected in the 280-THz band and C-band (near 190 THz) with additional EO combs (purple module). A fibre OFC with one comb tooth locked to a selected PDCS tooth (yellow module) enables optical frequency counting of the PDCS. All locks are referenced to a 10-MHz Rb standard. PM, phase modulator, SHG, second-harmonic generation. **b**, PDCS spectrum with harmonic pumps at $n_- = 261$ and $n_+ = 522$. The spectrum is normalized to 1 mW, that is, equivalent to dBm. **c**, Locked CEO beat spectrum referenced to the 10-MHz standard (inset, free-running CEO). RBW, resolution bandwidth. **d**, Locked ν_{rep}^{pdcs} detected at 280 THz (top) and in the C-band (bottom), verifying a single repetition rate across the PDCS spectrum. **e**, Allan deviation of the PDCS comb teeth ($n = 260$–265), showing the $1/\tau$ slope of synchronization to the microwave reference. Error bars represent one standard deviation. Right inset, schematic of the PDCS acting as a coherent microwave-to-optical link (shaded), measured with a fibre OFC. Left inset, Allan deviation of ν_{rep}^{pdcs} in the C-band. The deviation at $\tau < 10^{-1}$ s stems from the poor clocking of the EO comb microwave synthesizer. DUT, device under test. **f**, Frequency counting accuracy: measured PDCS comb teeth agree with expected values $\nu_{expected} = n\nu_{rep}^{pdcs} + \nu_{ceo}^{pdcs}$.

First, we demonstrate self-stabilization of our PDCS, in which both ν_{rep}^{pdcs} and ν_{ceo}^{pdcs} are locked to a microwave standard, enabling precise knowledge of all optical frequency comb teeth. We set the pump lasers at harmonic comb tooth modes ($n_+ = 2n_- = 522$) and measure the CEO before the chip from the tapped pumps, with an electro-optic comb (EO comb) downconverting the large $\nu_+ - 2\nu_-$ beat (Fig. 4a, Methods and Supplementary Information section 10). After generating the self-aligned PDCS, we lock the downconverted ν_{ceo}^{pdcs} to a 10-MHz rubidium microwave standard (Fig. 4c, inset) through feedback onto ν_+. At the output, we measure ν_{rep}^{pdcs} in the 280-THz band with another EO comb downconverter apparatus (Supplementary Information section 10) and lock it to the same 10 MHz reference (Fig. 4d), feeding back onto ν_-.

We verify that the self-aligned PDCS is stabilized to the microwave reference by confirming that ν_{rep}^{pdcs} is consistent across the OFC spectrum and that all comb teeth carry the same relative stability as the reference. First, we measure ν_{rep}^{pdcs} in the C-band (Methods) and confirm the same ν_{rep}^{pdcs} 130 comb teeth away from the lock point (Fig. 4d). The detected ν_{rep}^{pdcs} synchronizes to the microwave reference for long-term stability (Fig. 4e, inset), despite short-term discrepancies that originate from the EO comb downconversion apparatus, confirming the self-aligned PDCS has a single repetition rate pinned by the two pump lasers. We measure the long-term stability of the self-aligned PDCS comb teeth from $n = 260$ to $n = 265$ using a method akin to stability transfer[37] from the PDCS to a commercial fibre OFC (Methods). All selected PDCS comb teeth exhibit a $1/\tau$ Allan deviation slope (Fig. 4e), demonstrating the coherent link between the microwave and optical domains, and synchronization to the microwave reference. The modified Allan deviation shows a $1/\tau^{3/2}$ slope, confirming white phase noise and synchronization. We note that acquisition for the $n = 265$ comb tooth is shorter because of limited power available from the fibre-comb apparatus, resulting in a poorer long-term lock. Finally, we count the optical frequency of the comb teeth (Fig. 4f), which exhibit a Gaussian distribution centred around the expected value from the PDCS-locked values of ν_{rep}^{pdcs} and ν_{ceo}^{pdcs}.

Next, we demonstrate octave-separated optical two-point locking that enables coherent OFD from two locked optical tones onto the repetition rate of the self-aligned PDCS, which, with the same architecture, enables either low-noise millimetre-wave generation or optical clockwork operation (Fig. 5). Unlike narrow-band two-point locking schemes that typically pin two comb teeth separated by about 60 teeth through feedback to a single degree of freedom (the single pump)[34,35], our system provides two orthogonal degrees of freedom through the pump lasers, enabling complete stabilization of the repetition rate at the input side. Moreover, the octave separation maximizes the OFD factor to $n_+ = 522$ by incorporating the CEO into the two-point locking scheme, while simultaneously enabling long-term stabilization through clockwork operation and locking to a stable atomic transition within the same architecture. Hence, we operate with the same self-aligned PDCS as previously in Fig. 4, changing only the input laser lock point (Fig. 5a). In one case, before the chip, the CEO is locked similarly to the previous experiment through feedback onto one pump laser, whereas now the other remaining pump laser is locked to an integrated Si_3N_4 reference cavity[38] (Methods). In the other, both pump lasers are locked

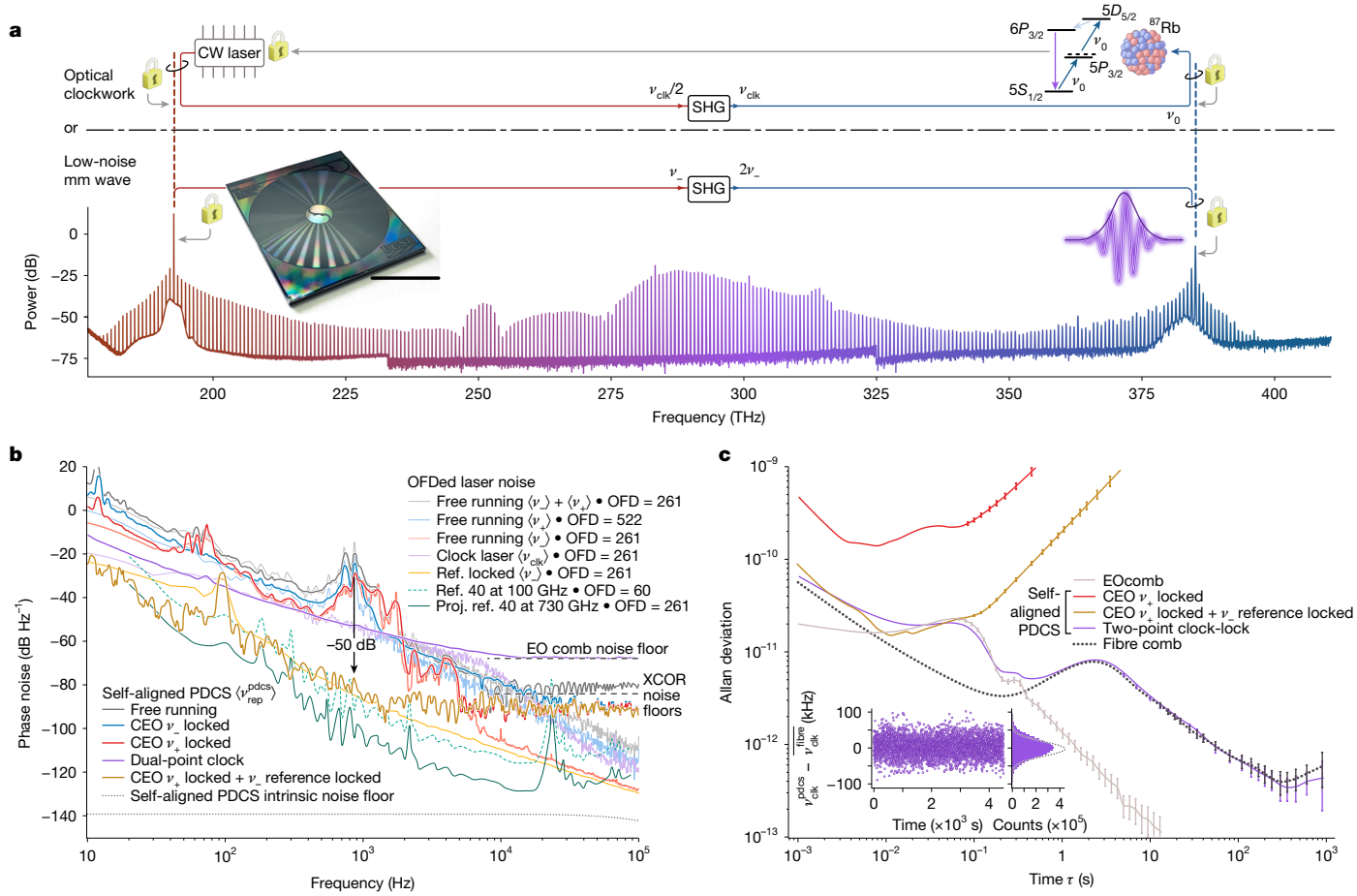


Fig. 5 | Optical-to-microwave link: low-noise millimetre-wave generation and optical clockwork operation. a, Experimental system. Using the same self-aligned PDCS as before, the system acts as a low-noise millimetre-wave generator or as an optical clockwork, depending only on the input laser locks. Power is normalized to 1 mW (dBm). **b**, PDCS repetition rate phase noise spectral power density $\langle\nu^{pdcs}_{rep}\rangle$ under different input laser configurations: free-running (grey), CEO locked with the negative (blue) or positive pump (red), both lasers locked to the clock laser and its second harmonic (purple), and CEO locked with positive pump and negative pump locked to a reference cavity (yellow). The corresponding laser noise divided by the expected OFD factor appears in matching colours, aligning with the PDCS repetition rate noise. Also shown for comparison are phase noise from ref. 40 (dashed green) and a projection of a self-aligned PDCS in a similar pump-lock configuration. The self-aligned PDCS photon-lifetime noise floor lies well below the projection (dotted black line). Phase noise densities are normalized to 1 mW (equivalent to dBc Hz^{-1}). **c**, Allan deviation for different locking configurations. Error bars represent one standard deviation. The free-running negative pump and CEO locked with positive pump configuration exhibits a rapid random frequency walk (red). The reference cavity-locked configuration, despite the best phase noise, drifts over time, leading to poor averaging for $\tau > 0.1$ s (yellow). The atomic-clock-locked PDCS demonstrates good long-term averaging (purple), matching for $\tau > 1$ s a commercial fibre OFC clockwork probing the same atomic transition (black dotted). The discrepancy between the fibre comb and PDCS at $\tau < 0.1$ s originates from the EO comb ν^{pdcs}_{rep} downconverter (grey). Bottom inset, clock frequency counted from the PDCS and fibre-comb repetition rates, ν^{pdcs}_{clk} and ν^{fibre}_{clk}. Both produce identical statistics, shown by the centred Gaussian distribution of ν^{pdcs}_{clk} against the fibre-comb average ν^{fibre}_{clk}. Scale bar, 1 cm (**a**).

to a continuous-wave laser and its second harmonic, with the latter being locked to the ^{87}Rb two-photon clock transition[39] (Methods).

We study the phase noise spectral density of the PDCS repetition rate $\langle\nu^{pdcs}_{rep}\rangle$. The PDCS divides down the laser noise ($\langle\nu_-\rangle$, $\langle\nu_+\rangle$ or both) onto $\langle\nu^{pdcs}_{rep}\rangle$ according to the dual-pinning configuration (Methods) (Fig. 5b). Once the CEO is locked by feedback to the positive pump laser ν_+ and the remaining negative pump laser ν_- is locked to an Si_3N_4 integrated reference cavity[38] to reduce its noise, the transduced $\langle\nu_{rep}\rangle$ exhibits the expected 50 dB reduction, demonstrating OFD operation of the self-aligned PDCS. Although we use cross-correlation detection of ν^{pdcs}_{rep}, reducing the detection noise by more than 25 dB (Methods and Supplementary Information section 9), the long-term frequency drift of the lasers prevents extended averaging. As a result, the noise floor exceeds the OFD of the laser noise above 10 kHz, which future work will improve. Despite this measurement floor, our performance at low Fourier frequencies already matches the state-of-the-art microcomb sources[40] using a similar integrated Si_3N_4 reference cavity[38], despite our intentionally conservative locking configuration and roughly seven times larger carrier frequency. An optimized cavity lock projects superior performance owing to our larger OFD factor, while remaining orders of magnitude above the self-aligned PDCS photon-lifetime noise floor (Supplementary Information section 1).

We next operate the same self-aligned PDCS as an optical clockwork, changing only the input laser to be locked to the ^{87}Rb-SH-stabilized continuous-wave laser, providing for frequency stability transfer[41] from the clock laser and its sub-harmonic onto the self-aligned PDCS. We note that the phase noise, which we confirm is transferred from the lasers onto ν^{pdcs}_{rep} by OFD, exceeds that of the reference-locked case (Fig. 5b), which follows from a lower signal-to-noise ratio of the weak ^{87}Rb two-photon fluorescence detection[42] compared with a Pound–Drever–Hall lock on our near-critically coupled cavity[38], decreasing the low-noise performance of the locked laser[43]. Thus, in our system, the atomic reference provides the long-term stability, and the cavity reference the short-term stability. To that end, we note that in both the free-running and cavity-reference-locked self-aligned PDCS cases, the Allan deviation rises rapidly after short averaging time τ, in the former

case from intrinsic laser drift, whereas in the latter case because of the thermal drift of the integrated reference cavity[38]. By contrast, it averages down in the clock-locked case (Fig. 5c) because of the good long-term stability of the atomic transition[39]. To confirm that the self-aligned PDCS acts as a true clockwork, we perform a second experiment a day later in which we locked the CEO and one comb tooth of a fibre comb to the clock laser, achieving identical Allan deviation performance except at $\tau < 1$ s, in which the PDCS repetition rate noise is dominated by the EO comb downconverter. We retrieve the measured clock frequency from both the PDCS ($\nu_{\mathrm{clk}}^{\mathrm{pdcs}}$) and fibre-comb ($\nu_{\mathrm{clk}}^{\mathrm{fibre}}$) clockworks (Methods) by repetition rate frequency counting. The PDCS shows a centred Gaussian frequency counting distribution (Fig. 5c, inset) offset from $\nu_{\mathrm{clk}}^{\mathrm{fibre}}$ by about 3 kHz, well within the approximately 26 kHz standard deviation for 75 min of statistics. Both clockworks exhibit a similar fixed offset from the accepted literature value of the transition, which we attribute to systematic shifts in the Rb two-photon apparatus (Methods).

Discussion

Our self-aligned PDCS microcomb operates significantly differently from standard DKS microcombs that rely on outward cascading from a centred single pump laser, which results in weak and noisy signals at the comb edges, thus complicating the CEO detection and locking required for precision metrology. In our self-aligned system, quasi-harmonic pumping determines the comb span and CEO of the subsequently generated PDCS before the chip, enabling robust operation. Moreover, intrinsic two-point locking from the two input pumps generating and trapping the PDCS enables octave-separated orthogonal control of all integrated OFC degrees of freedom. Thus, this new approach enables versatile, bidirectional reconfiguration of the same PDCS as a coherent bridge between the microwave and optical domains. We demonstrate the benefit of this versatility by performing three key tasks for integrated OFC systems: self-referencing to establish a stable frequency grid that can serve as a backbone for optical frequency synthesizers[27] or wavemeters[44], two-point optical locking (including the CEO) for low-noise millimetre-wave generation, and optical clockwork for transferring the relative stability of the ^{87}Rb atomic clock transition to the PDCS repetition rate.

Although at present detecting our large repetition rate requires a phase modulator apparatus for downconversion, this high repetition rate is an integral part of the architecture. For a self-referenced platform, a large repetition rate prevents pump power from being diluted into densely packed comb teeth spread across the entirety of the spectrum, most of which serve no metrological purpose. Pairing a large-repetition-rate comb with a separate narrow-band low-repetition-rate comb[27,28,45], in particular, in view of recent advances in power-efficient, low-repetition-rate DKS-based microcomb generation[23,46,47], for a second level of OFD[48] provides a SWaP-efficient path to field deployment, without the prohibitive pump power that an octave-spanning low-repetition-rate device would demand. Furthermore, with the recent improvement in integration of $\chi^{(2)}$ materials, integrated EO combs are also becoming a viable option for a low-SWaP, second OFD level[49]. Should fabrication advances eventually enable low-SWaP operation of a single octave-spanning comb at a low repetition rate, the benefits of our self-aligned PDCS concept would translate directly to that platform.

Moving forward, our self-aligned PDCS enables several integration capabilities, many arising from the stabilized, octave-separated pumps that remain available for further use. For example, the system is highly suitable for integrated SHG of the negative pump for high signal-to-noise ratio CEO detection. Available pump powers in the 10 mW range avoid the need for extremely high normalized conversion efficiency. Monolithic integration with photogalvanic-induced SHG in silicon nitride microresonators[50] is particularly compelling because it would enable a complete OFC clockwork in a single fabrication process. Moreover, nonlinear processes involving one or both pumps, whose frequencies are precisely known through PDCS self-stabilization, offer marked potential to generate stable continuous-wave reference tones outside the PDCS spectral window. Second- and third-harmonic generation and sum-frequency generation can enable interfacing with atomic systems used in quantum sensing[51,52] and higher-performance optical clocks[43,53,54]. Finally, although the PDCS centre frequency operates in the anomalous dispersion regime, both pumps reside in the normal dispersion regime. With appropriate dispersion engineering and pump-frequency selection, we expect self-aligned PDCS bandwidths to exceed the roughly one-octave limit thus far demonstrated with standard DKSs, and thus anticipate that ultra-broadband optical parametric oscillators recently demonstrated in the same silicon nitride platform[55] can be used for PDCSs. Conversely, we note that a self-aligned PDCS, in which the two pumps are no longer quasi-harmonically related in a low-repetition-rate resonator, is also physically possible based on numerical modelling (Supplementary Information section 1), particularly when leveraging recent advances in dispersion engineering[41,56,57], thus opening interesting avenues beyond self-referencing.

In conclusion, our self-aligned PDCS presents a foundry-compatible paradigm shift in integrated frequency metrology by inverting the architectural approach that has confined on-chip frequency combs to laboratory settings. Combined with rapid advances in laser[58,59] and modulator[49] integration, our scheme is a critical step in fulfilling the long-standing promise of field-deployable precision optical frequency combs for navigation, quantum technologies and fundamental physics measurements.

Online content

Any methods, additional references, Nature Portfolio reporting summaries, source data, extended data, supplementary information, acknowledgements, peer review information; details of author contributions and competing interests; and statements of data and code availability are available at https://doi.org/10.1038/s41586-026-11086-2.

1. Diddams, S. A., Vahala, K. & Udem, T. Optical frequency combs: coherently uniting the electromagnetic spectrum. *Science* **369**, eaay3676 (2020).
2. Kippenberg, T. J., Gaeta, A. L., Lipson, M. & Gorodetsky, M. L. Dissipative Kerr solitons in optical microresonators. *Science* **361**, eaan8083 (2018).
3. Li, Q. et al. Stably accessing octave-spanning microresonator frequency combs in the soliton regime. *Optica* **4**, 193–203 (2017).
4. Drake, T. E., Stone, J. R., Briles, T. C. & Papp, S. B. Thermal decoherence and laser cooling of Kerr microresonator solitons. *Nat. Photon.* **14**, 480–485 (2020).
5. Englebert, N. et al. Parametrically driven Kerr cavity solitons. *Nat. Photon.* **15**, 857–861 (2021).
6. Moille, G. et al. Parametrically driven pure-Kerr temporal solitons in a chip-integrated microcavity. *Nat. Photon.* **18**, 617–624 (2024).
7. Lombardi, M. A. Microsecond accuracy at multiple sites: is it possible without GPS? *IEEE Instrum. Meas. Mag.* **15**, 14–21 (2012).
8. Finkelstein, R. et al. Universal quantum operations and ancilla-based read-out for tweezer clocks. *Nature* **634**, 321–327 (2024).
9. Ye, J. & Zoller, P. Essay: quantum sensing with atomic, molecular, and optical platforms for fundamental physics. *Phys. Rev. Lett.* **132**, 190001 (2024).
10. Derevianko, A. et al. Fundamental physics with a state-of-the-art optical clock in space. *Quantum Sci. Technol.* **7**, 044002 (2022).
11. Dimarcq, N. et al. Roadmap towards the redefinition of the second. *Metrologia* **61**, 012001 (2024).
12. Metcalf, A. J. et al. Stellar spectroscopy in the near-infrared with a laser frequency comb. *Optica* **6**, 233–239 (2019).
13. Holzwarth, R. et al. Optical frequency synthesizer for precision spectroscopy. *Phys. Rev. Lett.* **85**, 2264–2267 (2000).
14. Fortier, T. M. et al. Generation of ultrastable microwaves via optical frequency division. *Nat. Photon.* **5**, 425–429 (2011).
15. Bruch, A. W. et al. Pockels soliton microcomb. *Nat. Photon.* **15**, 21–27 (2021).
16. Wu, T.-H. et al. Visible-to-ultraviolet frequency comb generation in lithium niobate nanophotonic waveguides. *Nat. Photon.* **18**, 218–223 (2024).
17. Del'Haye, P. et al. Phase-coherent microwave-to-optical link with a self-referenced microcomb. *Nat. Photon.* **10**, 516–520 (2016).
18. Hickstein, D. D. et al. Ultrabroadband supercontinuum generation and frequency-comb stabilization using on-chip waveguides with both cubic and quadratic nonlinearities. *Phys. Rev. Appl.* **8**, 014025 (2017).

19. Telle, H. R. et al. Carrier-envelope offset phase control: a novel concept for absolute optical frequency measurement and ultrashort pulse generation. *Appl. Phys. B* **69**, 327–332 (1999).
20. Jones, D. J. et al. Carrier-envelope phase control of femtosecond mode-locked lasers and direct optical frequency synthesis. *Science* **288**, 635–639 (2000).
21. Liu, J. et al. High-yield, wafer-scale fabrication of ultralow-loss, dispersion-engineered silicon nitride photonic circuits. *Nat. Commun.* **12**, 2236 (2021).
22. Ou, S.-C., Antohe, A. O., Carpenter, L. G., Moille, G. & Srinivasan, K. 300 mm wafer-scale SiN platform for broadband soliton microcombs compatible with alkali atomic references. *Opt. Lett.* **50**, 5578–5581 (2025).
23. Stern, B., Ji, X., Okawachi, Y., Gaeta, A. L. & Lipson, M. Battery-operated integrated frequency comb generator. *Nature* **562**, 401–405 (2018).
24. Sun, Y. et al. Applications of optical microcombs. *Adv. Opt. Photon.* **15**, 86–175 (2023).
25. Lucas, E., Guo, H., Jost, J. D., Karpov, M. & Kippenberg, T. J. Detuning-dependent properties and dispersion-induced instabilities of temporal dissipative Kerr solitons in optical microresonators. *Phys. Rev. A* **95**, 043822 (2017).
26. Brasch, V., Lucas, E., Jost, J. D., Geiselmann, M. & Kippenberg, T. J. Self-referenced photonic chip soliton Kerr frequency comb. *Light Sci. Appl.* **6**, e16202 (2017).
27. Spencer, D. T. et al. An optical-frequency synthesizer using integrated photonics. *Nature* **557**, 81–85 (2018).
28. Newman, Z. L. et al. Architecture for the photonic integration of an optical atomic clock. *Optica* **6**, 680–685 (2019).
29. Wu, K. et al. Vernier microcombs for high-frequency carrier envelope offset and repetition rate detection. *Optica* **10**, 626–633 (2023).
30. Moille, G., Shandilya, P., Stone, J., Menyuk, C. & Srinivasan, K. All-optical noise quenching of an integrated frequency comb. *Optica* **12**, 1020–1030 (2025).
31. Wu, K. et al. Vernier microcombs for integrated optical atomic clocks. *Nat. Photon.* **19**, 400–406 (2025).
32. Menyuk, C. R., Shandilya, P., Courtright, L., Moille, G. & Srinivasan, K. Multi-color solitons and frequency combs in microresonators. *Opt. Express* **33**, 21824–21835 (2025).
33. Moille, G. et al. Kerr-induced synchronization of a cavity soliton to an optical reference. *Nature* **624**, 267–274 (2023).
34. Papp, S. B. et al. Microresonator frequency comb optical clock. *Optica* **1**, 10–14 (2014).
35. Kudelin, I. et al. Photonic chip-based low-noise microwave oscillator. *Nature* **627**, 534–539 (2024).
36. Diakonov, A., Khrizman, K., & Stern, L., Hybrid-locked Kerr microcombs for flexible on-chip optical clock division. Preprint at https://doi.org/10.48550/arXiv.2508.07258 (2025).
37. Lucas, E. et al. Ultralow-noise photonic microwave synthesis using a soliton microcomb-based transfer oscillator. *Nat. Commun.* **11**, 374 (2020).
38. Liu, K. et al. 36 Hz integral linewidth laser based on a photonic integrated 4.0 m coil resonator. *Optica* **9**, 770–775 (2022).
39. Martin, K. W. et al. Compact optical atomic clock based on a two-photon transition in rubidium. *Phys. Rev. Appl.* **9**, 014019 (2018).
40. Sun, S. et al. Integrated optical frequency division for microwave and mmWave generation. *Nature* **627**, 540–545 (2024).
41. Lucas, E., Yu, S.-P., Briles, T. C., Carlson, D. R. & Papp, S. B. Tailoring microcombs with inverse-designed, meta-dispersion microresonators. *Nat. Photon.* **17**, 943–950 (2023).
42. Beard, R., Martin, K. W., Elgin, J. D., Kasch, B. L. & Krzyzewski, S. P. Two-photon rubidium clock detecting 776 nm fluorescence. *Opt. Express* **32**, 7417–7425 (2024).
43. Ludlow, A. D., Boyd, M. M., Ye, J., Peik, E. & Schmidt, P. O. Optical atomic clocks. *Rev. Mod. Phys.* **87**, 637–701 (2015).
44. Niu, R. et al. kHz-precision wavemeter based on reconfigurable microsoliton. *Nat. Commun.* **14**, 169 (2023).
45. Briles, T. C. et al. Interlocking Kerr-microresonator frequency combs for microwave to optical synthesis. *Opt. Lett.* **43**, 2933–2936 (2018).
46. Shen, B. et al. Integrated turnkey soliton microcombs. *Nature* **582**, 365–369 (2020).
47. Helgason, Ó. B. et al. Surpassing the nonlinear conversion efficiency of soliton microcombs. *Nat. Photon.* **17**, 992–999 (2023).
48. Ou, S.-C. et al. Passive interlocking of W-band repetition rate and octave-spanning microcombs toward giant on-chip optical frequency division. In *Proc. Conference on Lasers and Electro-Optics (CLEO)* STh1B.2 (Optica Publishing, 2026).
49. He, Y. et al. Chip-scale high-performance photonic microwave oscillator. *Sci. Adv.* **10**, eado9570 (2024).
50. Clementi, M., Zatti, L., Zhou, J., Liscidini, M. & Brès, C.-S. Ultrabroadband milliwatt-level resonant frequency doubling on a chip. *Nat. Commun.* **16**, 6164 (2025).
51. Saffman, M., Walker, T. G. & Mølmer, K. Quantum information with Rydberg atoms. *Rev. Mod. Phys.* **82**, 2313–2363 (2010).
52. Pak, C., Schlitters, M. J. & Bergeson, S. D. Improved ionization potential of calcium using frequency-comb-based Rydberg spectroscopy. *Phys. Rev. A* **106**, 062818 (2022).
53. Nicholson, T. L. et al. Systematic evaluation of an atomic clock at 2×10^{-18} total uncertainty. *Nat. Commun.* **6**, 6896 (2015).
54. Zhang, C. et al. Frequency ratio of the ^{229m}Th nuclear isomeric transition and the ^{87}Sr atomic clock. *Nature* **633**, 63–70 (2024).
55. Sun, Y. et al. Advancing on-chip Kerr optical parametric oscillation towards coherent applications covering the green gap. *Light Sci. Appl.* **13**, 201 (2024).
56. Moille, G., Lu, X., Stone, J., Westly, D. & Srinivasan, K. Fourier synthesis dispersion engineering of photonic crystal microrings for broadband frequency combs. *Commun. Phys.* **6**, 144 (2023).
57. Yuan, Z. et al. Soliton pulse pairs at multiple colours in normal dispersion microresonators. *Nat. Photon.* **17**, 977–983 (2023).
58. Prokoshin, A., Gehl, M., Madaras, S., Chow, W. W. & Wan, Y. Ultra-narrow-linewidth hybrid-integrated self-injection locked laser at 780 nm. *Optica* **11**, 1024–1029 (2024).
59. Ji, X. et al. Wafer-scale manufacturing of ultra-broadband, high-power erbium-doped integrated lasers. *Nat. Commun.* **17**, 3722 (2026).

Publisher's note Springer Nature remains neutral with regard to jurisdictional claims in published maps and institutional affiliations.

© This is a U.S. Government work and not under copyright protection in the US; foreign copyright protection may apply 2026

Methods

Device design and fabrication

The devices were fabricated at the commercial silicon nitride foundry Ligentec, in which a 100-mm (4-inch) wafer is patterned with a repeated 22 mm × 22 mm reticle containing the 1.8 mm × 5.4 mm chip with the microring designs of interest. The photonic devices are created through a subtractive process, in which the Si_3N_4 atop a SiO_2 layer is removed to create the design, and then encapsulated in a top SiO_2 layer. The microring geometry, namely, the ring width RW and Si_3N_4 thickness H, is chosen for optimal dispersion conditions in which the OPO condition and phase-matching with the PDCS occur simultaneously at the octave-apart pump frequencies $\nu_{\pm}$. Specifically, the OPO condition results in minimization of the frequency mismatch $2\Delta\nu(n) = [\nu_{res}(n_+) + \nu_{res}(n_-)] - [\nu_{res}(n) + \nu_{res}(n_+ + n_- - n)]$ at the centre mode $2n_0 = n_- + n_+$ (±1 when n_- is odd), where ν_{res} are the resonance frequencies and $n_{\pm}$ are the pumped modes. The self-alignment condition requires minimization of the phase velocity mismatch between the PDCS and its pumps, achieved when the PDCS-integrated dispersion, $D_{int}(n) = \nu_{res}(n) - \left[\frac{\nu_{res}(n_+) + \nu_{res}(n_-)}{2} + nD_1\right]$, is close to zero at both pumps, in which our definitions of D_{int} and D_1 have units of linear and not angular frequency. This minimizes the frequency offsets $\Delta\nu_{ceo}$, with small residual offsets compensated by pump-frequency tuning to reach efficient PDCS self-alignment. These conditions essentially reduce to minimizing odd-order dispersion to obtain symmetric PDCS-integrated dispersion that crosses zero at the two octave-separated pumps. A bus waveguide of width W_{wg}, tapered to 200 nm at the facet for edge coupling to lensed fibres, is wrapped in a pulley configuration[60] around the microring with a gap G between the bus and ring. The choice of the pulley length L_c allows for chromatic dispersion engineering of the coupling quality factor Q_c across the octave, such that the positive pump and the PDCS centre frequencies are critically coupled ($Q_c \approx Q_0$), whereas the negative pump is largely overcoupled ($Q_0 \gg Q_c$). See Supplementary Information section 2 for details. The in-plane parameters, such as G and RW, are varied throughout the chip to compensate for fabrication imperfections and provide some lithographic tuning of the PDCS properties.

Results in Figs. 2, 4 and 5 used two different devices, both on the same wafer with an H = 660 nm Si_3N_4 film. The device ring radius is RR = 31 μm, corresponding to an FSR of about 735 GHz, exhibiting intrinsic quality factor $Q_0 \approx 1.5 \times 10^6$ and coupling quality factor $Q_c(\nu_+) \approx Q_c((\nu_+ + \nu_-)/2) \approx 1.5 \times 10^6$ and $Q_c(\nu_-) \approx 4 \times 10^4$ (Supplementary Information section 6). The devices in Figs. 2, 4 and 5 are coupled to a W_{wg} = 500 nm bus waveguide wrapped around the ring at gap G = 400 nm with a pulley length L_c = 17 μm. The two devices differ only in their ring width: the device of Fig. 2 has RW = 850 nm, while the device used in Figs. 4 and 5 has RW = 860 nm. The devices used for Fig. 3 share the same microring geometry (RR = 23 μm, RW = 850 nm) but are fabricated on a different wafer with an Si_3N_4 film thickness of H = 680 nm. The coupling conditions are varied from device to device, with pulley lengths L_c = 15 μm, 17 μm, 18 μm and 19 μm, bus waveguide widths W_{wg} = 450 nm, 460 nm and 470 nm, and gaps G = 400 nm, 450 nm and 500 nm, such that the correct combination yields the appropriate coupling condition at the frequencies of interest, as described above, and yields similar Q factors to the RR = 31 μm designs. Different coupling configurations change the coupling chromatic dispersion and hence the spectral extraction of the PDCS across the octave, resulting in different output spectra, while not affecting the generation nor the self-alignment of the PDCS state. Across the sampled devices, the required ν_- frequency adjustment spans about 130 GHz (about 150 GHz for ν_{ceo}^{pdcs}), which the integrated heaters compensate through the thermo-optic shift.

PDCS generation protocol

To generate the PDCS, the two pump lasers ν_- and ν_+ are set to the transverse electric (TE) polarization on injection on-chip to pump the fundamental mode of the microring resonator (TE_0). First, the positive pump ν_+ is set on resonance; given its near-visible wavelength, it can be directly observed through residual scattering captured by the optical vision apparatus, in addition to transmission spectroscopy. The negative pump ν_- thus remains on the blue-detuned side of its resonance. Working with ν_+ first and parking it offers the main advantage that because it operates at a shorter wavelength, the residual absorption and resulting heat generated by this laser exceed that of ν_- (which is in the C-band). This choice prevents complex nonlinear behaviour of the frequency detunings of the pumps relative to their resonances, and this dual-pump operation, similar to the auxiliary laser approach used for thermo-optic stabilization in standard DKS generation[61,62], provides intrinsic thermal compensation for temperature stabilization (Supplementary Information section 3) and direct adiabatic access to the PDCS state. The negative pump is then set close to its resonance, with its piezoelectric element sweeping slowly (20 Hz) across a span of about 40 GHz. A fibre wavelength demultiplexer enables probing of the PDCS power without interference from the pump powers (Fig. 1b, inset).

Overcoupling of the ν_- resonance offers two main advantages for PDCS generation: it reduces the thermal impact of the ν_- laser (relative to the fixed ν_+ laser) and enables very large frequency tuning while remaining on resonance. Therefore, any frequency discrepancy in the OPO condition for PDCS generation and/or frequency tuning necessary for self-alignment can be compensated while maintaining ν_- on resonance. This makes PDCS generation extremely robust, as it is simply obtained by adiabatic (that is, manual tuning of the laser actuator) frequency tuning of ν_-, and once accessed, the PDCS remains stable over time (over a working day in the self-aligned regime), without active feedback to the lensed fibres or pump lasers. Supplementary Information section 4 shows that the PDCS, outside its self-alignment window, can be maintained for >2 GHz frequency detuning of ν_-.

Nonlinear dynamics data acquisition

Once the PDCS is generated through the protocol described above, we characterize the self-synchronization presented in Fig. 2 and Supplementary Information section 6. The resonator operates in a small dispersive regime within the bandwidth of interest between ν_- and ν_+, in which the nonlinearity suffices to lock the group velocity between the soliton and any pumped component[6]. Outside synchronization, the only degree of freedom within the resonator is the phase velocity mismatch, which leads to frequency interleaving of the PDCS and the pumped components. This offset $\Delta\nu_{ceo}$ is equal in magnitude but opposite in sign between the PDCS and the ν_+ component and the PDCS and the ν_- component. Once synchronized, all phases lock, creating a single frequency grid with a single CEO. To determine synchronization, we measure $\Delta\nu_{ceo}$ and its vanishing when self-alignment occurs. The pumped component and PDCS spectra overlap throughout the spectrum, which becomes apparent when working in a soliton crystal state, in which the different components can be segregated based on their interleaving (Supplementary Information section 5). We detect $\Delta\nu_{ceo}$ by filtering the complete spectrum around 300 THz (that is, 980 nm) using a wavelength demultiplexer (WDM) and a 6-GHz photodiode. We reconstruct the spectrogram by measuring the temporal signal of $\Delta\nu_{ceo}$ while sweeping ν_-. Using the `scipy.signal` Python package, we reconstruct the temporal spectrogram. We calibrate the negative pump detuning $\delta\nu_-$ by similarly creating a spectrogram of the heterodyne signal between ν_- and a 125-MHz fibre optical frequency comb. A similar procedure is used for the positive pump detuning ν_+. The non-zero phase-locking window means that the soliton self-adapts to maintain the synchronization condition whereas the repetition rate can undergo a frequency shift. Therefore, ν_{rep}^{pdcs} is also disciplined in the self-aligned PDCS case. We measure ν_{rep}^{pdcs} using an EO comb downconversion scheme similar to ref. 30. This consists of two cascaded phase modulators that are overdriven by a microwave synthesizer at ν_{rf}^{rep} to

create many sidebands. By modulating two adjacent PDCS comb teeth around 280 THz so that each generates sidebands that span at least $\nu_{rep}^{pdcs} \approx 735$ GHz, the mth sideband from the two PDCS comb teeth will be offset from each other by a frequency ν_{IF}^{rep} within the photodiode detection bandwidth (50 MHz). The EO comb thus acts as a local oscillator, enabling frequency downconversion of ν_{rep}^{pdcs} into a detectable frequency $\pm\nu_{IF}^{rep} = \nu_{rep}^{pdcs} - m\nu_{rf}^{rep}$. The sign is determined by whether the modulated PDCS sidebands cross before the overlap; in our case, they are always set to avoid a crossing (that is, positive sign). Because of the linear relationship between the repetition rate ν_{rep}^{pdcs} and its frequency-downconverted signal ν_{IF}^{rep}, we can directly map $\partial\nu_{IF}^{rep}/\partial\nu_{\pm} = \partial\nu_{rep}^{pdcs}/\partial\nu_{\pm}$ as we keep the EO comb fixed. Similarly to $\Delta\nu_{ceo}$, we record the temporal signal of ν_{IF}^{rep} while sweeping $\delta\nu_{-}$ and reconstruct the spectrogram.

Microwave-to-optical link experiment

Self-stabilization of the PDCS is achieved by phase-locking the repetition rate ν_{rep}^{pdcs} and the CEO frequency ν_{ceo}^{pdcs}. To set ν_{ceo}^{pdcs}, we double the negative pump ν_{-} through SHG before the PDCS chip and beat it against the positive pump ν_{+}. Because the PDCS self-aligns to the two pump lasers, both pumps are comb teeth; performing this measurement on the input side is thus analogous to standard f–$2f$ nonlinear interferometry for CEO retrieval, but is done before the comb is generated, is intrinsically low-noise (that is, only the two lasers contribute, with no impact from the microring cavity or PDCS intrinsic noise) and exhibits a very large signal-to-noise ratio. For setting ν_{ceo}^{pdcs}, the two lasers are tapped from the input using respective 10% couplers (without amplification), and we obtain $P_{2\nu-} \approx 10$ μW and $P_{\nu+} \approx 1$ mW. As ν_{ceo}^{pdcs} is large, its detection is performed using an EO comb apparatus consisting of one phase modulator acting on the positive pump laser to frequency-downconvert ν_{ceo}^{pdcs} to a 10-MHz beat note such that $\nu_{IF}^{ceo} = \nu_{ceo}^{pdcs} - p\nu_{rf}^{ceo}$ (p is the number of electro-optic sidebands). We phase-lock ν_{IF}^{ceo} to an Rb 10 MHz microwave reference, which serves as the input reference for all microwave synthesizers throughout the setup, by feedback to the positive pump laser. We measure the frequency-downconverted repetition rate ν_{IF}^{rep} in the 280 THz spectral band and lock it to the same 10 MHz reference. The same downconversion scheme is replicated with a third EO comb to independently detect ν_{rep}^{pdcs} in the C-band. From both locks, we determine the expected PDCS comb tooth frequencies such that $\nu_{expected}(n) = n\nu_{rep}^{pdcs} + \nu_{ceo}^{pdcs} = n(\nu_{IF}^{rep} + m\nu_{rf}^{rep}) + \nu_{IF}^{ceo} + p\nu_{rf}^{ceo}$. Although we used an electro-optic phase modulator because of the specific device large ν_{ceo}^{pdcs}, our self-aligned PDCS architecture also permits ring radius engineering—a standard approach in octave-spanning systems[63]—which we demonstrate in our platform in Supplementary Information section 8. When taken in combination with the thermal tuning shown in Fig. 3, this enables ν_{ceo}^{pdcs} to be brought to a desired value, potentially close to zero.

We measure an individual PDCS comb tooth frequency and stability using a commercial fibre optical frequency comb with repetition rate $\nu_{rep}^{fibre} \approx 125$ MHz. We leverage the coherent two-way bridge between optical and microwave frequencies to count the PDCS comb teeth. Although we could self-reference the fibre comb by locking its CEO and repetition rate, and then heterodyne one fibre-comb tooth against one PDCS tooth, the noise multiplication from this upstream scheme produces excessive noise in the fibre-comb teeth given the modest noise performance of our Rb 10 MHz microwave reference, rendering this frequency counting impossible. Instead, we leverage OFD. In this scheme, the downconverted CEO of the PDCS, ν_{IF}^{ceo}, and the CEO of the fibre comb, ν_{ceo}^{fibre}, are both locked to the same Rb 10 MHz microwave reference. One fibre-comb tooth is then phase-locked to one PDCS tooth at a frequency offset δ_{lock} referenced to the same Rb reference. By directly detecting and counting ν_{rep}^{fibre}, we retrieve the PDCS comb tooth frequency and stability with $\nu_{meas}(n) = k\nu_{rep}^{fibre} + \nu_{ceo}^{fibre} \pm \delta_{lock}$, where k is the fibre-comb tooth order that locks to the PDCS, and the sign before the lock offset depends on the mode number. The measurements presented in Fig. 4 are performed deliberately with different ν_{ceo}^{pdcs} and ν_{rep}^{pdcs} conditions by actuating the pump laser, demonstrating that the self-aligned PDCS comb teeth are predictable regardless of the self-stabilization operating point.

Optical-to-microwave link experiment

We use the same self-aligned PDCS as in the microwave-to-optics experiment, but modify the locks of the input lasers. In one scenario to generate low-noise millimetre-waves, we set the CEO of the PDCS similarly by doubling the input negative laser and beating it against the input positive laser, followed by phase-locking the EO frequency-downconverted tone to a 10-MHz reference with feedback on either laser depending on the scheme. The remaining laser can either remain free or be locked to a reference cavity. When the CEO is locked through ν_{+}, we use an integrated 10 m coiled-spiral microcavity reference made of Si_3N_4 and embedded in SiO_2, similar to that used in ref. 38, and packaged with direct fibre pigtail access. Using a Pound–Drever–Hall technique, in which the input laser ν_{-} is phase-modulated at 25 MHz, the laser locks to the dip of the high-Q resonance of the integrated cavity reference. For noise measurement, the repetition rate ν_{rep}^{pdcs} is detected in the same fashion as before, namely, using EO combs as local oscillators to frequency-downconvert the repetition rate into a detected window. However, as with every local oscillator downconversion scheme, the noise of the EO comb imprints on the detected beat note such that $\langle\nu_{IF}^{rep}\rangle = \langle\nu_{rep}^{pdcs}\rangle + N\langle\nu_{rf}^{rep}\rangle$. To bypass the noise floor from the EO comb detection, we detect ν_{rep}^{pdcs} simultaneously in the 280 THz and C-band spectral windows with two independent EO combs and microwave synthesizers. The two downconverted beats enable a cross-correlation (XCOR) measurement, removing the uncorrelated noise from each EO comb and decreasing the noise floor by approximately 25 dB compared with single EO comb ν_{rep}^{pdcs} detection. This noise floor can be further reduced with larger XCOR averaging, which in our setup is at present limited by ν_{rep}^{pdcs} frequency drift from the reference cavity frequency drift, as seen in the Allan deviation characterization in Fig. 5c. The PDCS repetition rate noise follows the dual-pinning configuration of the input lasers. Free-running pump lasers lead to $\langle\nu_{rep}^{pdcs}\rangle = (\langle\nu_{-}\rangle + \langle\nu_{+}\rangle)/n_{-}$. Locking the CEO on the negative pump leads to $\langle\nu_{rep}^{pdcs}\rangle = \langle\nu_{+}\rangle/n_{+}$, whereas locking the CEO on the positive pump leads to $\langle\nu_{rep}^{pdcs}\rangle = \langle\nu_{-}\rangle/n_{-}$. It is assumed that the CEO locking noise is negligible because it is further optically frequency divided, $\langle\nu_{ceo}^{pdcs}\rangle/n_{\pm}$.

For the clockwork measurement, the clock laser is phase-modulated and stabilized using fluorescence detection from the ^{87}Rb vapour cell, analogous to PDH locking but detecting incoherent fluorescence instead of transmitted light, with lock-in amplifier and servo feedback, in an apparatus similar to that in ref. 42. We retrieve the clock frequency from the PDCS using $\nu_{clk}^{pdcs} = 2(n_{-}\nu_{rep}^{pdcs} + \delta_{-} - \delta_{+}) = 2[n_{-}(\nu_{IF}^{rep} + m\nu_{rf}^{rep}) + \delta_{-} - \delta_{+}]$, where $\delta_{-} = \nu_{-} - \nu_{clk}/2 = 46{,}334{,}200$ kHz and $\delta_{+} = \nu_{+} - \nu_{clk} = -160{,}092{,}120.004$ kHz are the locked offsets of the two pumps from the clock input. We determine these offsets accurately by phase-locking and frequency downconversion of the pump-clock beat notes using respective EO combs (see Supplementary Information section 10). We measured the repetition rate $\nu_{rep}^{pdcs} = (737{,}302{,}133.41 \pm 0.05)$ kHz over 75 min, yielding $\nu_{clk}^{pdcs} = 385{,}284{,}566{,}278 \pm 26$ kHz. We retrieve the fibre-comb clock frequency from $\nu_{clk}^{fibre} = k\nu_{rep}^{fibre} + \nu_{ceo}^{fibre} + \delta_k$ with $\delta_k = 35$ MHz the locked offset of the kth comb tooth from the clock input, $\nu_{ceo}^{fibre} = -15$ MHz, $k = 3{,}082{,}212$, and the measured $\nu_{rep}^{fibre} = 125{,}002.611$ kHz ±7 mHz. This leads to $\nu_{clk}^{fibre} = (385{,}284{,}566{,}275 \pm 20)$ kHz. Compared with the published two-photon ^{87}Rb transition frequency of ($\nu_{clk} = 385{,}284{,}566{,}370.400 \pm 10$) kHz (refs. 28,64–68), in which the standard deviation represents the average across all the references, the PDCS-determined clock laser frequency exhibits an offset of $\nu_{clk}^{pdcs} - \nu_{clk} = (-92 \pm 31)$ kHz and the fibre-comb-determined clock frequency is $\nu_{clk}^{fibre} - \nu_{clk} = (-95 \pm 25)$ kHz. Hence, both OFCs exhibit similar offsets, with a discrepancy from each other that is well within their

respective standard deviations. The observed clock frequency offset is attributed to systematic effects in the vapour cell. Vapour density may exceed temperature-based estimates from resistance temperature detectors because of temperature gradients in the compact geometry used in this experiment. ^{87}Rb–^{87}Rb collisional shifts, which scale exponentially with temperature, can contribute tens of kHz of frequency shift. Atom-wall collisions probably contribute more significantly in this smaller cell than in larger cells, although these effects remain poorly characterized. Importantly, this shift does not compromise operational performance as observed in the Allan deviation in Fig. 5c.

Data availability

The data that support the plots within this paper and other findings of this study are available from the corresponding authors upon request.

Code availability

The simulation code used for the Lugiato–Lefever and thermal modelling presented in this work is available from the corresponding authors upon request.

60. Moille, G. et al. Broadband resonator-waveguide coupling for efficient extraction of octave-spanning microcombs. *Opt. Lett.* **44**, 4737–4740 (2019).
61. Zhou, H. et al. Soliton bursts and deterministic dissipative Kerr soliton generation in auxiliary-assisted microcavities. *Light Sci. Appl.* **8**, 50 (2019).
62. Zhang, S. et al. Sub-milliwatt-level microresonator solitons with extended access range using an auxiliary laser. *Optica* **6**, 206–212 (2019).
63. Zang, J., Liu, H., Briles, T. C. & Papp, S. B. Foundry manufacturing of octave-spanning microcombs. *Opt. Lett.* **49**, 5143–5146 (2024).
64. Nez, F., Biraben, F., Felder, R. & Millerioux, Y. Optical frequency determination of the hyperfine components of the 5S12-5D32 two-photon transitions in rubidium. *Opt. Commun.* **102**, 432–438 (1993).
65. Hilico, L. et al. Metrological features of the rubidium two-photon standards of the BNM-LPTF and Kastler Brossel Laboratories. *Eur. Phys. J. Appl. Phys.* **4**, 219–225 (1998).
66. Bernard, J. E. et al. Absolute frequency measurement of a laser at 1556 nm locked to the $5S_{1/2}$- $5D_{5/2}$ two-photon transition in ^{87}Rb. *Opt. Commun.* **173**, 357–364 (2000).
67. Edwards, C. S., Barwood, G. P., Margolis, H. S., Gill, P. & Rowley, W. R. C. Development and absolute frequency measurement of a pair of 778 nm two-photon rubidium standards. *Metrologia* **42**, 464 (2005).
68. Zhang, S. Y. et al. Direct frequency comb optical frequency standard based on two-photon transitions of thermal atoms. *Sci. Rep.* **5**, 15114 (2015).

Acknowledgements Any mention of commercial products within this article is for information only; it does not imply recommendation or endorsement by the National Institute of Standards and Technology nor the US government. Approved for public release, distribution is unlimited. Public Affairs release approval no. AFRL-2026-0416. The views expressed are those of the authors and do not reflect the official policy or position of the US government. We thank K. D. Nelson of Honeywell Aerospace Technologies for help with fabrication of the silicon nitride coil resonator. We thank S. Fatema and Z. Newman for their feedback.

Author contributions G.M., M.E. and K.S. conceptualized the project. G.M., P.S. and M.E. developed the theoretical framework with help from Z.L. and C.R.M.; G.M. designed the resonators. S-C.O. helped with initial device linear characterization. M.H., K.L. and D.J.B. designed and fabricated the integrated reference cavity. R.B., R.R. and S.P.K. developed the Rb atomic clock system. G.M. led the project and performed the measurements as single operator, and completed most of the analysis. J.S. helped with the metrology analysis. G.M., M.E. and K.S. wrote the paper, with input from all co-authors. All the authors contributed to and discussed the content of this paper.

Funding G.M., J.S. and K.S. acknowledge partial funding support from the Space Vehicles Directorate of the Air Force Research Laboratory and the NIST-on-a-chip and IMS programs of the National Institute of Standards and Technology. G.M., K.S. and M.E. acknowledge partial funding support from the Marsden Fund of the Royal Society Te Apārangi (grant no. 23-UOA-071) and from the Quantum Technologies Aotearoa Programme. P.S. and C.R.M. acknowledge support from collaborative agreement nos. 2022138-142232 and 2023200-142386 with the National Center for Manufacturing Sciences as sub-awards from US DoD cooperative agreements HQ0034-20-2-0007 and HQ0034-24-2-0001 and from NIST contract 60NANB24D106. D.J.B. acknowledges funding from the DARPA MTO Gryphon program under award no. HR0011-22-2-0008.

Competing interests G.M., M.E. and K.S. have submitted a provisional patent application based on aspects of the work presented in this paper. The other authors declare no competing interests.

Additional information
Supplementary information The online version contains supplementary material available at https://doi.org/10.1038/s41586-026-11086-2.

Correspondence and requests for materials should be addressed to Grégory Moille or Kartik Srinivasan.

Peer review information *Nature* thanks Shun Fujii and the other, anonymous, reviewer(s) for their contribution to the peer review of this work. Peer reviewer reports are available.

Reprints and permissions information is available at http://www.nature.com/reprints.

nature portfolio

https://doi.org/10.1038/s41586-026-11086-2

Supplementary information

Self-aligned optical microcomb emerging between octave-separated lasers

In the format provided by the authors and unedited

Supplementary Information: Self-aligned optical microcombs emerging between octave separated lasers

Grégory Moille,[1,2,*] Pradyoth Shandilya,[3] Jordan Stone,[2] River Beard,[4] Shao-Chien Ou,[1,2] Zongda Li,[5,6] Mark Harrington,[7] Kaikai Liu,[7] Robert Rockmore,[8] Curtis R. Menyuk,[3] Daniel J. Blumenthal,[7] Sean P. Krzyzewski,[8] Miro Erkintalo,[5,6] and Kartik Srinivasan[1,2,†]

[1] *Joint Quantum Institute, NIST/University of Maryland, College Park, USA*
[2] *Microsystems and Nanotechnology Division, National Institute of Standards and Technology, Gaithersburg, USA*
[3] *University of Maryland Baltimore County, Baltimore, MD, USA*
[4] *AV Incorporated, Albuquerque, New Mexico, USA*
[5] *Department of Physics, University of Auckland, Auckland 1010, New Zealand*
[6] *The Dodd-Walls Centre for Photonic and Quantum Technologies, New Zealand*
[7] *Department of Electrical and Computer Engineering, University of California Santa Barbara, Santa Barbara, CA, USA*
[8] *Air Force Research Laboratory, Space Vehicles Directorate, Kirtland Air Force Base 87117, USA*

(Dated: July 20, 2026)

Contents

S.1. Numerical investigation of self-aligned PDCSs 2
S.2. Pulley coupler chromatic dispersion 3
S.3. Impact of temperature and thermo-refractive dispersion 4
S.4. Unsynchronized PDCS repetition rate dependence with pump detuning 4
S.5. PDCS-crystal states and PDCS envelope extraction 5
S.6. Robustness of the self-aligned PDCS for wafer-scale compatibility 6
S.7. Thermal tuning of self-aligned PDCS 8
S.8. Carrier envelope offset engineering with ring radius 8
S.9. Cross correlation measurement of the repetition rate 9
S.10. Complete experimental apparatus 9
References 11

* gmoille@umd.edu
† kartik.srinivasan@nist.gov

S.1. Numerical investigation of self-aligned PDCSs

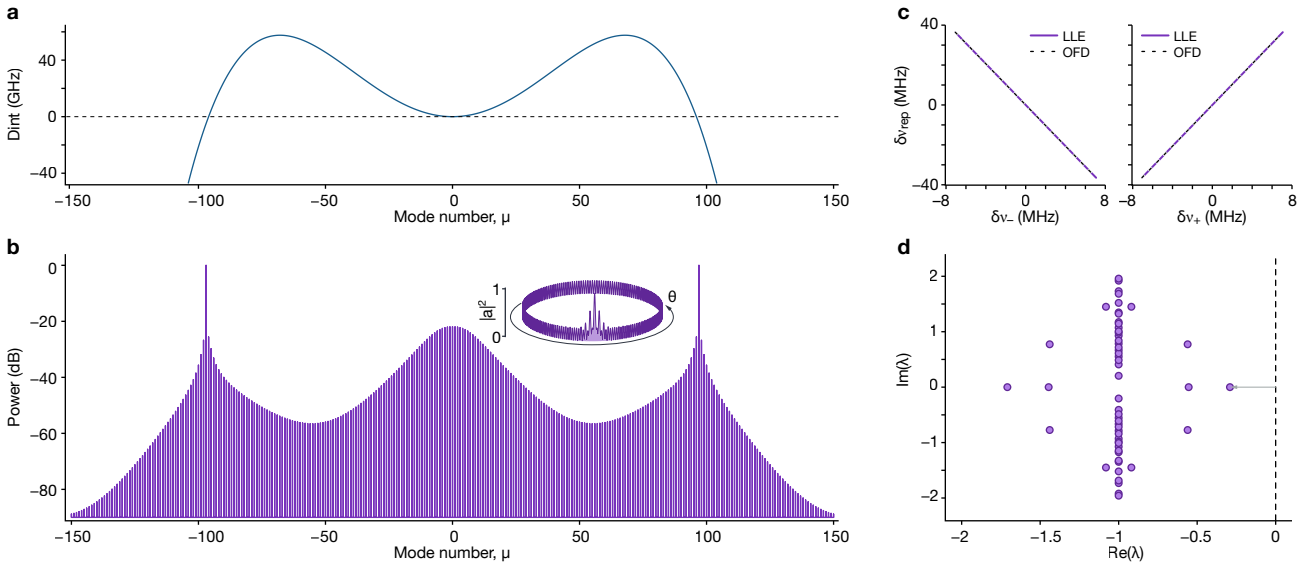


Fig. S.1 – Numerical study of self-aligned PDCS— **a** Integrated dispersion profile $D_{\mathrm{int}}(\mu)$ used in the numerical simulations where only the even order dispersion terms are considered. The dispersion is chosen such that $D_{\mathrm{int}}(\mu_{\pm}) \approx 0$ at the pumped modes $\mu_{\pm} = \pm 97$. **b** Simulated self-aligned PDCS spectrum. The intracavity field azimuthal profile is shown in the inset. **c** Repetition rate variation of the PDCS ($\delta\nu_{\mathrm{rep}}^{\mathrm{pdcs}}$) as a function of the negative (left) and positive (right) pump detuning variation $\delta\nu_{\pm}$. The solid lines are the simulation results and the dashed lines the expected disciplining from the optical frequency division between the two pumps. **d** Eigenvalue spectrum of the linearized operator corresponding to the self-aligned PDCS solution. The arrow represents the position-shifting eigenvalue (Goldstone mode) that has become negative, indicating the symmetry breaking, and hence synchronization to the pumps.

To study numerically the generation and self-alignment of the PDCS, we use the multi-pumped Lugiato-Lefever equation (LLE):[1]

$$\frac{\partial a(\theta,t)}{\partial t} = -\frac{\kappa}{2}a + i\sum_{\mu} 2\pi D_{\mathrm{int}}(\mu)A(\mu)e^{i\mu\theta} + i|a|^2 a + \sqrt{\kappa_{\mathrm{ext}}P_-}\exp\left\{i\left[2\pi\delta\nu_- + 2\pi D_{\mathrm{int}}(\mu_-)\right]t + i\mu_-\theta\right\} + \sqrt{\kappa_{\mathrm{ext}}P_+}\exp\left\{i\left[2\pi\delta\nu_+ + 2\pi D_{\mathrm{int}}(\mu_+)\right]t + i\mu_+\theta\right\}, \tag{S.1}$$

with $a(\theta,t)$ the intracavity field profile along the resonator angle θ and time t, κ the cavity loss rate, $D_{\mathrm{int}}(\mu)$ is the integrated dispersion computed at $(\mu_- + \mu_+)/2$ (i.e., at the spectral center of the PDCS) and has units of frequency (not angular frequency), $P_{\pm}$ the negative and positive pump power, $\delta\nu_{\pm}$ the pump detunings from their respective cavity resonances, and $\mu_{\pm}$ the mode numbers of the pumps relative to the center of the PDCS. The other parameters are defined in the main text. We chose symmetric conditions with $\mu_+ = -\mu_- = 97$ to ensure the integrated dispersion $D_{\mathrm{int}}(\mu_{\pm})$ approaches zero at the two pumped modes. We account only for even-order dispersion terms, such that $D_{\mathrm{int}}(\mu) \equiv (D_2/2)\mu^2 + (D_4/24)\mu^4$ (Fig. S.1a). This approach renders the integrated dispersion and OPO frequency matching condition identical.

Currently, an understanding of the full phase space of PDCSs and their various excitation pathways remains under exploration.[2] Therefore, we assume the single PDCS as an initial condition and allow it to evolve in time, governed by Eq. (S.1), to confirm that the PDCS is indeed a stable solution of the system. From this evolution, we extract the intracavity field profile, consisting of a single pulse with periodic modulation from the beating between the two pumps that travel at the same group and phase velocity, along with its spectrum (Fig. S.1b). To verify the self-alignment, we proceed similarly to the experiment and scan the negative pump detuning $\delta\nu_-$ while keeping the positive pump detuning $\delta\nu_+$ fixed, and vice versa. First, we observe that the PDCS remains stable over the range of detunings studied. Second, the PDCS repetition rate variation $\delta\nu_{\mathrm{rep}}^{\mathrm{pdcs}}$ changes linearly with the pump detuning variation and the modal separation between the two pumps, as expected from optical frequency division (Fig. S.1c). We note that the LLE is FSR agnostic, and all the dispersion profiles presented here are as a function of the mode number. Therefore, as long as such dispersion can be produced, regardless of the cavity size, a PDCS and more specifically, a self-aligned PDCS, can exist.

We study the stability of the PDCS by linearizing Eq. (S.1) around the PDCS solution and finding the eigenvalues λ of the linearized operator, following the approach in Ref.[3] and described in more detail in Refs..[4,5] We observe that the position-shifting eigenvalue (the Goldstone mode) λ_{ps} becomes negative, confirming the symmetry breaking and

self-alignment of the PDCS (Fig. S.1d). From this linear analysis, we can define a Langevin equation, assuming the exponential damping of the fluctuation of the repetition rate:

$$\frac{\partial \Delta\nu_{\mathrm{rep}}^{\mathrm{pdcs}}}{\partial t} = \frac{1}{2\pi}\left(\lambda_{\mathrm{ps}}\kappa + \eta_T \frac{d\Delta T}{\partial t}\right) \tag{S.2}$$

with η_T the variation of repetition rate against temperature and the temperature fluctuation defined by another Langevin equation,

$$\frac{d\Delta T}{\partial t} = -\Gamma_T \Delta T + \zeta_T \tag{S.3}$$

where Γ_T is the thermal dissipation rate and ζ_T is a white-noise fluctuation source defined by its autocorrelation,

$$\langle \zeta_T(t)\zeta_T(t+\tau)\rangle = \frac{\Gamma_T k_{\mathrm{B}} T^2}{\rho C V}\delta(\tau) \tag{S.4}$$

with k_{B} the Boltzmann constant, T the cavity temperature, ρ the Si_3N_4 density, C the specific heat, and Γ_T the thermal dissipation rate; detailed parameter values for the cavity appear in Refs.[3,6–8]

Taking the Fourier transform of Eq. (S.2), we obtained the power spectral density of the self-aligned PDCS repetition rate $\nu_{\mathrm{rep}}^{\mathrm{pdcs}}$ noise,

$$S(f) = 2\frac{k_B T \eta_T^2 \Gamma_T}{\rho C V\,(f^2+\Gamma_T^2)} \times \frac{f^2}{f^2+\lambda_{\mathrm{ps}}^2\kappa^2} \tag{S.5}$$

The Goldstone mode λ_{ps} can reach a minimum value of -1, establishing a photon-lifetime-limited noise floor for Fourier frequencies f below the photon lifetime inverse (κ), and the spectrum of Eq. (S.5) is displayed in Fig. 5b

S.2. Pulley coupler chromatic dispersion

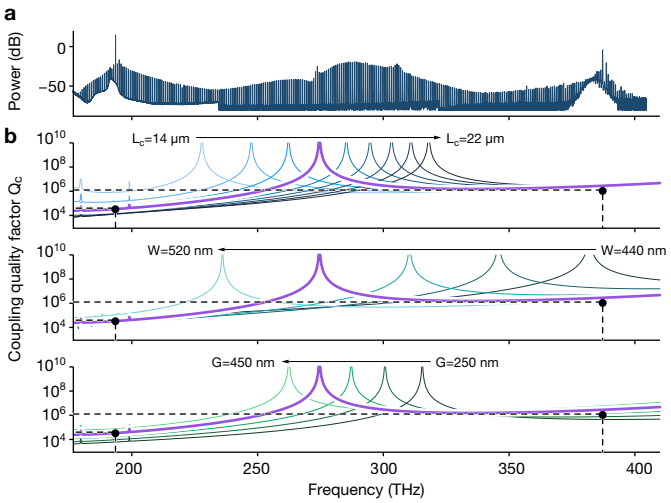


Fig. S.2 – Pulley-coupler chromatic dispersion engineering for PDCS generation— **a** Self-aligned PDCS spectra for $RW = 850$ nm presented in Fig. 1. The pulley coupler characteristics of these devices, and the other RW tested in Section S.6 are $G = 400$ nm, $L_c = 17$ μm, and $W = 500$ nm, resulting in a coupling quality factor at the pump of $Q_c(\nu_-) \approx 40 \times 10^3$ and $Q_c(\nu_+) \simeq 1.2 \times 10^6$, which is overcoupled and critically-coupled respectively.**b** Finite element method simulations of the pulley coupling quality factor against the frequency for a waveguide with the nominal dimensions but varying pulley length (top), varying waveguide width (center), and varying gap size (bottom). The purple trace in the three subplots corresponds to the nominal design used in the experiments. The dashed lines and circles correspond to the two pumps and their respective targeted coupled quality factor.

For efficient PDCS generation and self-alignment to octave-apart pump lasers, the chromatic dispersion of the microring coupling to a bus waveguide is critical. Although optimization for lowering the degenerate-OPO threshold and optimizing the coupling in every band of interest is still a very active research topic,[9,10] we find that for robust self-aligned PDCS generation the two pumps must be simultaneously injected into the microring resonator with high efficiency for effective nonlinear interaction, while providing sufficient frequency tunability to satisfy both the OPO condition and the self-alignment frequency offset condition. To achieve this, we design the bus waveguide to couple to the microring resonator in a pulley-like configuration, which exploits the phase mismatch between the bus and the microring resonator to engineer the chromatic dispersion of the coupling quality factor Q_c. In all devices tested in this manuscript that yield a self-aligned PDCS (see Section S.6), the pulley coupler consists of a bus waveguide (with Si_3N_4 thickness equal to that of the ring) with a width of $W = 500$ nm, wrapped around the ring over a pulley length of $L_c = 17$ μm, and separated by a gap of $G = 400$ nm. This coupler enables over-coupling at the ν_- pump while maintaining critical coupling at the ν_+ pump, providing greater flexibility in PDCS generation and self-alignment

while remaining efficient and allowing for on-chip pump powers approaching or below one hundred milliwatt. We note that our two pumps are an octave apart, making the pulley coupler extremely robust against fabrication uncertainty. One can first assume that the pulley length remains relatively accurately fabricated. A variation of waveguide width of ±20 nm results in the same coupling regime at both pumps, while gap variation has limited impact on the coupling (Fig. S.2).

S.3. Impact of temperature and thermo-refractive dispersion

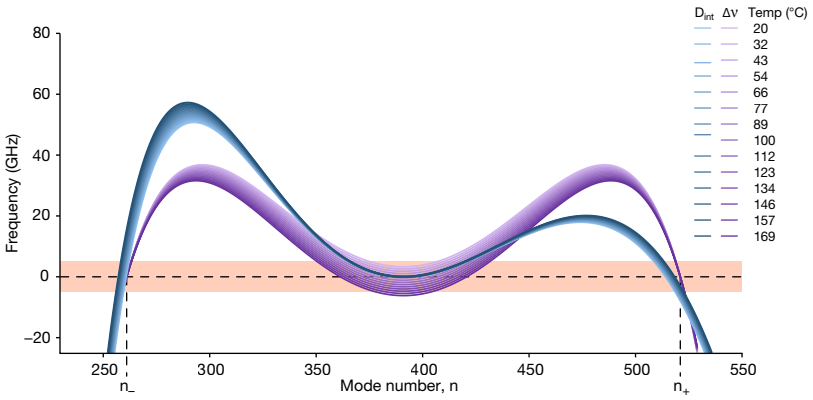


Fig. S.3 – Temperature dependence of phase matching for PDCS generation and self-alignment— Using finite-element method (FEM) simulations, we compute the OPO frequency mismatch $\Delta\nu$ (varying purple shades) and the integrated dispersion at the PDCS spectral center $D_{\rm int}$ (varying blue shades) as a function of resonator temperature. The increase of temperature, happening due to residual absorption of the pumps, leads to a negative shift in $\Delta\nu$, enabling phase-matching for PDCS generation. However, the integrated dispersion $D_{\rm int}$ does not change significantly, enabling the PDCS to remain self-aligned over the temperature range studied.

Here, we discuss the impact of resonator temperature on PDCS generation and self-alignment. As with standard DKSs, the on-chip pump powers and residual absorption of the Si_3N_4 resonator increase the resonator temperature. Although thermal bistability is generally a detriment for stably accessing DKS states with a single pump laser, it does not hinder PDCS generation and self-alignment. In particular, we do not implement frequency sweeping faster than the thermal lifetime to counter thermal bistability. Although the system is dual-pumped, we do not believe it operates in an identical fashion to laser-cooling and thermo-optic stabilization of microresonators that enable easier DKS access.[11,12] Indeed, the negative pump is very largely over-coupled, so its contribution to the thermal load is minimal compared to the positive pump, and no backaction mechanism stabilizes the resonator temperature. However, the positive pump is critically coupled and operated near visible wavelengths where Si_3N_4 absorption is larger, leading to a significant thermal load that red-shifts the resonator modes. In addition, the large frequency span of interest here (from 1550 nm to 775 nm) means that the mode overlap between the Si_3N_4 microring resonator core and the SiO_2 cladding—two materials with different thermo-refractive coefficients—varies significantly with wavelength, leading to effective thermo-refractive chromatic dispersion. We numerically model the impact of temperature change from room temperature (20 °C) to 169 °C on the resonator dispersion using finite-element method (FEM) simulations, extracting the integrated dispersion at the PDCS spectral center $D_{\rm int}$ and the OPO frequency mismatch $\Delta\nu$ [Fig. S.3]. We observe the behavior of $\Delta\nu$ close to the degenerate-OPO mode $(n_- + n_+)/2$, and find that it starts at positive values at room temperature and becomes smaller with increased temperature, eventually crossing zero and becoming negative. This indicates that the OPO condition shifts slightly between the cold cavity during linear measurements and the hot cavity when laser pumps are injected. This shift explains the slight positive offset of the OPO conditions for the device of interest (Fig. 2a and Fig. S.6). Importantly, within the temperature range studied, $D_{\rm int}$ does not change significantly, and the two pumps remain close to a working point of $D_{\rm int}(M_\pm) \approx 0$, enabling the PDCS to become self-aligned.

One important note is that the over-coupling of the pump resonances in the ν_- band, and the resulting large linewidths, enables large frequency tuning of the OPO and self-alignment conditions. This makes self-aligned PDCS generation robust in overcoming both fabrication-induced offsets from the target geometry and undesirable thermal effects that might otherwise be a limitation.

S.4. Unsynchronized PDCS repetition rate dependence with pump detuning

Although we focus the main text on the self-aligned PDCS, we also study the repetition rate dependence of an unsynchronized PDCS with respect to negative pump detuning variation $\delta\nu_-$. In this regime, the repetition rate variation $\delta\nu_{\rm rep}^{\rm pdcs}$ is not expected to follow the optical frequency division relation because the PDCS is not synchronized to the pumps. We observe that the repetition rate $\nu_{\rm rep}^{\rm pdcs}$ increases as $\delta\nu_-$ decreases (Fig. S.4), opposite to the self-aligned PDCS case (see Fig. 2). Further work is underway to understand this behavior. We probe the unsynchronized PDCS over a detuning range exceeding 2 GHz and limit the range only to ensure PDCS stability during measurement. This flexibility and robustness against negative pump detuning stems directly from the over-coupling regime of the negative pump resonance, which exhibits a linewidth of nearly 5 GHz. We note that the PDCS repetition rate exhibits

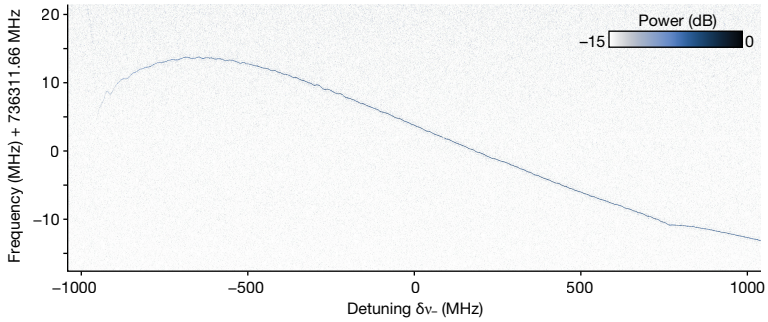


Fig. S.4 – Repetition rate dependence on the negative pump of the unsynchronized PDCS— Repetition rate spectrogram of the unsynchronized PDCS as a function of the negative pump detuning variation ($\delta\nu_-$) across more than 2 GHz.

a turning point near $\delta\nu_- \approx -600$ Hz, which may prove valuable for future low-noise microwave generation applications and pump noise rejection.

S.5. PDCS-crystal states and PDCS envelope extraction

Experimentally, we find that our octave-spanning PDCS, under appropriate pump conditions, which we find empirically to be primarily determined by the pump powers, can emerge as a crystal state, where multiple PDCSs are equally azimuthally spaced within the microring resonator [Fig. S.5]. In particular, we generate a 2-PDCS-crystal state using the 840 nm ring width device by pumping at modes $n_- = 265$ and $n_+ = 523$ (*i.e.*, 195.2 THz and 385.2 THz). Since each PDCS can exist with either a 0 or π phase,[13,14] we repeat the experiment until the two PDCS are both in phase, observable through a bright peak at $n_0 = (n_- + n_+)/2$. However, since $n_0 - n_- = n_+ - n_0$ is odd, the two pumps are spectrally placed at dark teeth of the PDCS crystal spectrum. This configuration enables straightforward extraction of the pump microcomb spectrum by selecting every other tooth from the total spectrum (top spectrum and markers in Fig. S.5b). This post-processing capability reveals spectral features previously hidden by the pump microcombs, most notably the PDCS dispersive wave. The extracted dispersive wave frequency aligns precisely with the phase-matching condition predicted by the integrated dispersion $D_{\rm int}$ (Fig. S.5a), confirming the theoretical understanding of PDCS generation. Beyond fundamental interest, this ability to separate PDCS and pump-generated spectral components through crystal-state engineering provides an additional degree of freedom for tailoring the output spectrum for specific applications, particularly where isolated PDCS spectral coverage is desired without pump laser contributions.

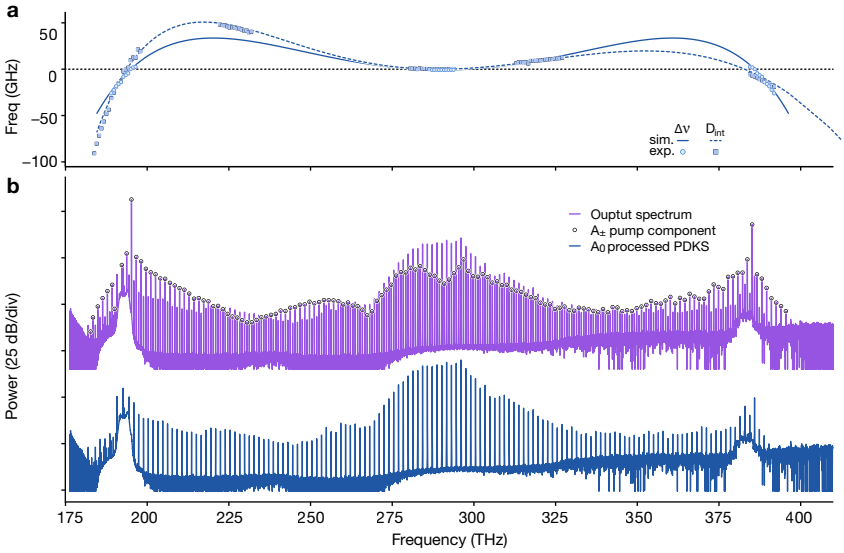


Fig. S.5 – PDCS crystal for post-processing out pump components— **a** Integrated dispersion $D_{\rm int}(\mu)$ (dashed) and OPO frequency mismatch $\Delta\nu$ (solid) for a device with 840 nm ring width. **b** Under appropriate pump conditions, determined primarily by pump power, a two-PDCS-crystal structure emerges (top purple). In such a scenario, the PDCS crystal and the microcomb generated by cross-phase modulation around the pumps are offset by one mode, in addition to being slightly offset from one another outside the self-alignment region. This configuration enables straightforward extraction of the pump microcomb (top markers), which can be subtracted from the total spectrum to retrieve the PDCS envelope (bottom blue). This procedure reveals the PDCS dispersive wave previously obscured by the pump microcombs and confirms alignment with the phase-matching condition predicted by $D_{\rm int}$.

S.6. Robustness of the self-aligned PDCS for wafer-scale compatibility

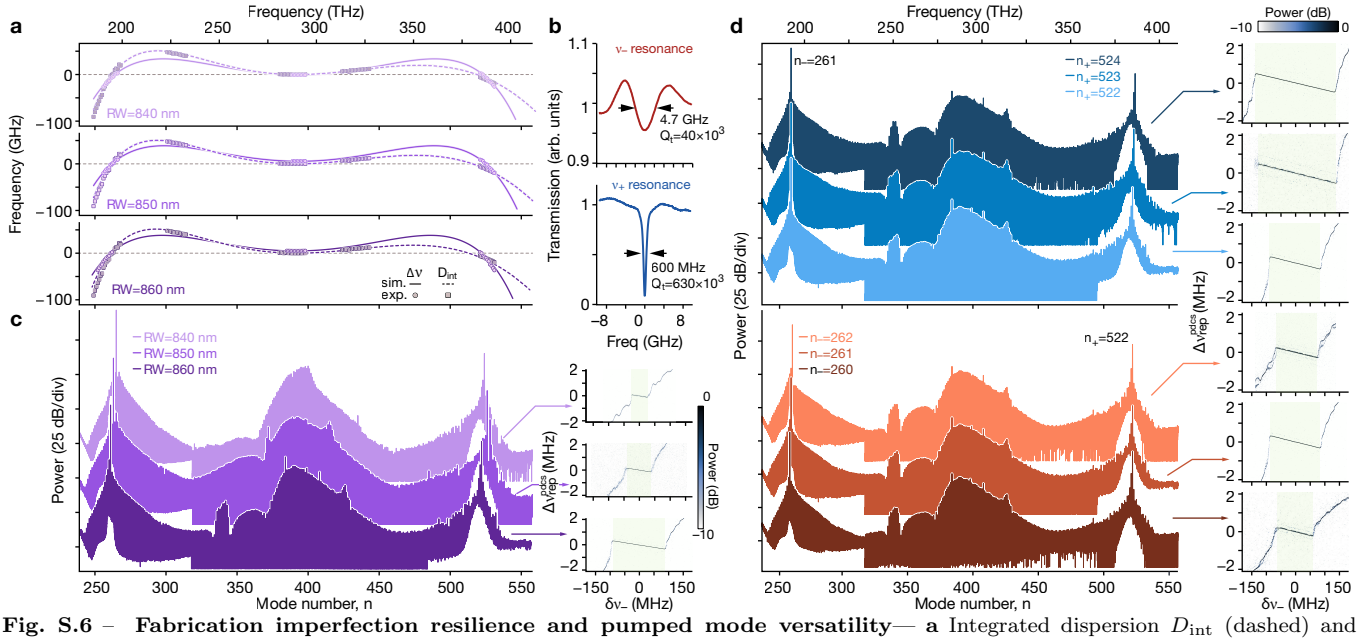


Fig. S.6 – Fabrication imperfection resilience and pumped mode versatility— **a** Integrated dispersion D_{int} (dashed) and OPO frequency mismatch $\Delta\nu$ (solid) for three different devices with slightly different ring widths (840 nm, 850 nm, and 860 nm) with experimental data (markers) in agreement with simulation (lines). **b** Measured pumped resonance spectra for the 860 nm ring width device. The negative pump resonance is strongly overcoupled, with a loaded quality factor $Q_{\mathrm{t}} \approx 40 \times 10^3$, while the positive pump resonance is nearly critically coupled, with $Q_{\mathrm{t}} \approx 640 \times 10^3$. The overcoupling of the negative pump resonance enables large detuning tolerance for PDCS generation and self-alignment. **c** Measured PDCS spectra for the three different devices when pumping at harmonic modes. **d** Measured PDCS spectra for the 860 nm ring width device pumped at different modes for both the positive (top) and negative (bottom) pumps. All the spectrograms shown to the right of the PDCS spectra in (c)-(d) show self-alignment through disciplining of the repetition rate variation $\Delta\nu_{\mathrm{rep}}^{pdcs}$ against the negative pump detuning $\delta\nu_-$.

A critical aspect of our self-aligned PDCS platform is its compatibility with foundry fabrication processes. Although foundry-fabricated devices exhibit high quality, they still contain fabrication imperfections that cause deviations from intended design parameters. Therefore, resilience to fabrication imperfections constitutes a critical criterion for deployable integrated OFC platforms. To assess this resilience, we investigate multiple devices fabricated during the same run. We observe that all devices with similar geometry—ring widths from $RW = 840$ nm to $RW = 860$ nm, corresponding to approximately 3 % variation—produce quasi-harmonic self-aligned PDCS with the correct dispersion condition (Fig. S.6a-c). We implemented additional ring widths in the same fabrication run, but the limited span available for the positive pump (due to the taper amplifier gain bandwidth) prevented testing of all devices. In addition, all three tested devices exhibited excellent tolerance against pump mode variation (Fig. S.6d), which was again limited only by the available pump laser wavelength range. An important contribution to this large tolerance is the chromatic dispersion of the coupling using the pulley coupler,[15] which critically couples the positive pump for efficient power transfer to the cavity and leverages a large effective nonlinear coefficient at short wavelengths,[16] while over-coupling the negative pump (Fig. S.6b). The latter is crucial because it allows the PDCS to exist over a very large negative pump frequency detuning, enabling the system to overcome fabrication imperfections, frequency mismatch, and dispersion offset.

e devices studied above use a microring radius of $RR = 31$ µm ($H = 660$ nm Si_3N_4 thickness), yielding an FSR of approximately 735 GHz, of which only two reticle fields were available, precluding a full-wafer study. To extend the robustness assessment to the wafer scale, we fabricated a second wafer with a Si_3N_4 thickness of 680 nm and a microring radius of $RR = 23$ µm ($RW = 850$ nm), yielding an FSR of approximately 1 THz. This design change also demonstrates that self-aligned PDCS generation is not restricted to a single FSR. For this geometry, all reticle fields across the full 100 mm wafer are available. However, not all chips within each field could be characterized: some dies are missing and others are defective (metal residue, damaged facets), and these are highlighted in white in the wafer map of **??**a. While the above establishes robustness against ring width and pumped mode variations on a single chip, demonstrating foundry compatibility requires additionally verifying self-alignment across coupling variations, chip-to-chip differences within a field, across independent fabrication runs (Fig. S.7), and across a full 100 mm wafer (**??**). The four complementary experiments presented here systematically isolate these remaining variables. In all cases (**??** and Fig. S.7), devices are pumped at the same modes around $\nu_- \approx 192.9$ THz (1555 nm) and $\nu_+ \approx 385.7$ THz

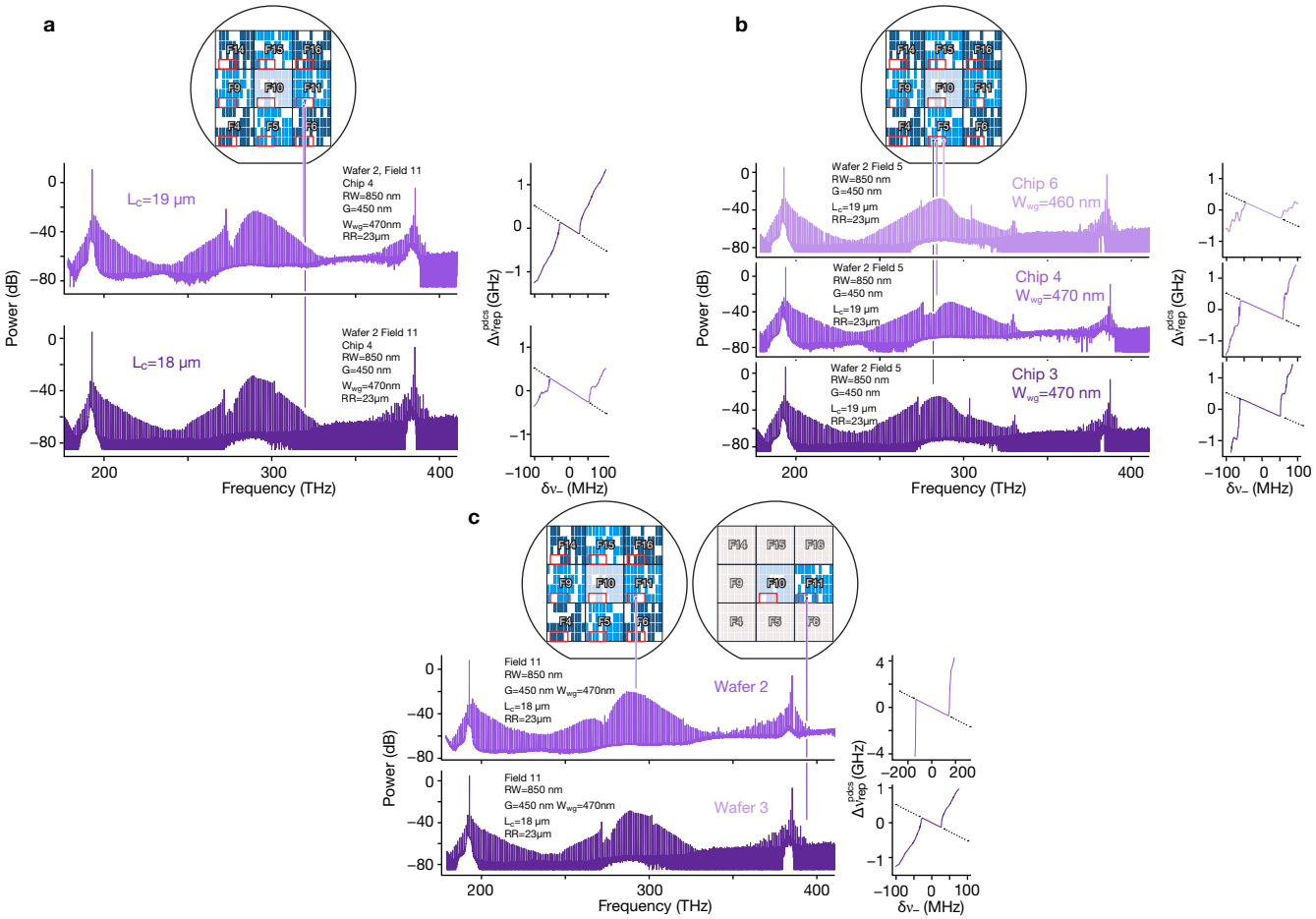


Fig. S.7 – **Additional wafer-scale compatibility measurements**— All devices use $RW = 850$ nm, $RR = 23$ μm (680 nm Si_3N_4 thickness, FSR ≈ 1 THz) and are pumped at $\nu_- \approx 192.9$ THz and $\nu_+ \approx 385.7$ THz. Each panel shows the wafer layout with each field (F) representing a repetitive pattern made of 44 individual chips, of which only the ones highlighted by the red rectangles correspond to microrings for PDCS generation. The blue shade corresponds to the average thickness across the field (light: 677 nm, medium: 680 nm and dark 683 nm). The missing or defective dies are represented in white. For each device tested, we measure their optical spectrum (left) and the corresponding repetition rate disciplining $\delta\nu_{\mathrm{rep}}^{\mathrm{pdcs}}$ vs. $\delta\nu_-$ (right), with the dashed line indicating the expected OFD=193 slope. **a** Same chip (Wafer 2, Field 11, Chip 4), same ring and coupler ($G = 450$ nm, $W_{\mathrm{wg}} = 470$ nm), varying pulley length: $L_{\mathrm{c}} = 19$ μm (top) and $L_{\mathrm{c}} = 18$ μm (bottom). **b** Same field (Wafer 2, Field 5), same ring and pulley length ($L_{\mathrm{c}} = 19$ μm, $G = 450$ nm), varying bus waveguide width chip-to-chip: Chip 6 ($W_{\mathrm{wg}} = 460$ nm, top), Chip 4 ($W_{\mathrm{wg}} = 470$ nm, middle), Chip 3 ($W_{\mathrm{wg}} = 460$ nm, bottom). **c** Same nominal design (Field 11, $G = 450$ nm, $W_{\mathrm{wg}} = 470$ nm, $L_{\mathrm{c}} = 18$ μm), two fabrication runs: Wafer 2 (top) and Wafer 3 (bottom), both 680 nm thickness.

(777.8 nm). In Fig. S.7a, we test two devices on the same chip (Wafer 2, Field 11, Chip 4) with identical ring geometry ($RW = 850$ nm, $RR = 23$ μm) and coupler parameters ($G = 450$ nm, $W_{\mathrm{wg}} = 470$ nm), varying only the pulley length: $L_{\mathrm{c}} = 19$ μm (top) and $L_{\mathrm{c}} = 18$ μm (bottom). Both devices yield self-aligned PDCS, demonstrating robustness against pulley length variation. In Fig. S.7b, we test three chips at different positions within the same reticle field (Wafer 2, Field 5), all sharing the same ring geometry ($RW = 850$ nm, $RR = 23$ μm) and pulley length ($L_{\mathrm{c}} = 19$ μm, $G = 450$ nm), with the bus waveguide width varying chip-to-chip: $W_{\mathrm{wg}} = 460$ nm (Chip 6, top), $W_{\mathrm{wg}} = 470$ nm (Chip 4, middle), and $W_{\mathrm{wg}} = 460$ nm (Chip 3, bottom). All three chips yield self-aligned PDCS, confirming within-field reproducibility against chip-to-chip bus waveguide width variation. In Fig. S.7c, we compare devices with identical nominal design (Field 11, $RW = 850$ nm, $RR = 23$ μm, $G = 450$ nm, $W_{\mathrm{wg}} = 470$ nm, $L_{\mathrm{c}} = 18$ μm) across two fabrication runs of the same design: Wafer 2 (top) and Wafer 3 (bottom), both with 680 nm Si_3N_4 thickness. The two devices yield near-identical self-aligned PDCS, confirming run-to-run reproducibility. Finally, the full-wafer sweep in **??**a uses a fixed ring geometry ($RW = 850$ nm, $RR = 23$ μm) throughout, with all devices pumped at approximately 192.9 THz (1555 nm) and 385.7 THz (777.8 nm). Missing die and chip-to-chip bus waveguide width variations within each field preclude a uniform coupling design across the full wafer; the coupling robustness demonstrated in panels a–c above ensures these unavoidable variations do not prevent self-aligned PDCS generation. The combination of these four tests presented in Fig. S.7 and **??** constitutes a realistic, non-idealized test of foundry compatibility.

S.7. Thermal tuning of self-aligned PDCS

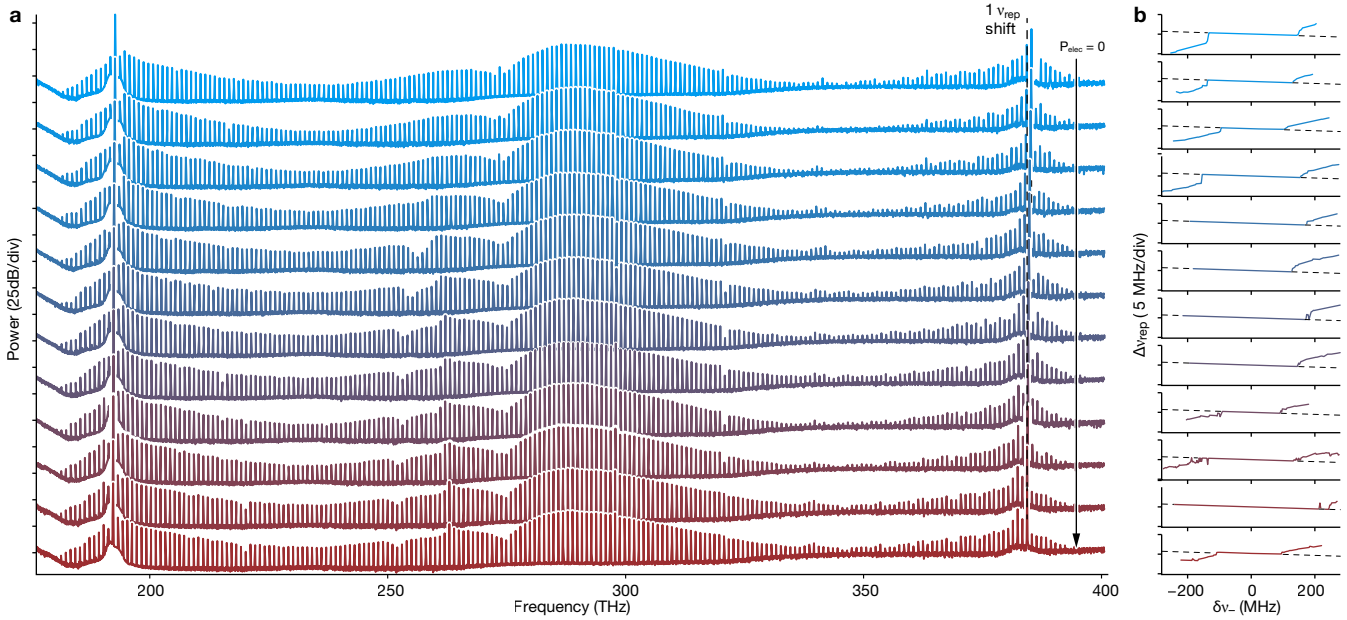


Fig. S.8 – Thermal tuning of self-aligned PDCS. a, Optical spectra of the self-aligned PDCS at quasi-harmonic pump settings, recorded at heater powers P_{elec} stepped from 0 to 135 mW (blue to dark red), with the integrated heater shown in Fig. 1b of the main text. Colors match those used in Fig. 3b–d of the main text. The positive pump tunes by more than one $\nu_{\mathrm{rep}}^{\mathrm{pdcs}}$. **b,** Repetition rate variation $\Delta\nu_{\mathrm{rep}}^{\mathrm{pdcs}}$ as a function of negative pump detuning $\delta\nu_{-}$ at each power, color-coded to match **a** and Fig. 3b–d of the main text. The OFD disciplining slope is recovered at every operating point, confirming that self-alignment is maintained across the full thermal tuning range.

The integrated heater shown in Fig. 1b of the main text, with a nominal resistance of $\approx 100\ \Omega$, enables thermal tuning of the self-aligned PDCS. We step the electrical power P_{elec} from 0 to 135 mW in coarse ≈ 10 mW increments, regenerating the PDCS and finding the self-alignment condition at each step. Both pumps red-shift via the thermo-optic effect, and since $\nu_{+} \approx 2\nu_{-}$, the positive pump tunes by approximately twice the negative pump, covering more than one $\nu_{\mathrm{rep}}^{\mathrm{pdcs}}$ (Fig. S.8a). The OFD disciplining slope is recovered at each power (Fig. S.8b), confirming self-alignment across the full tuning range. A continuous control interface combining fine power stepping with programmed pump-frequency tracking would maintain self-alignment without regeneration, enabling fine alignment of either pump to a reference of interest such as a high-finesse cavity or atomic transition.

S.8. Carrier envelope offset engineering with ring radius

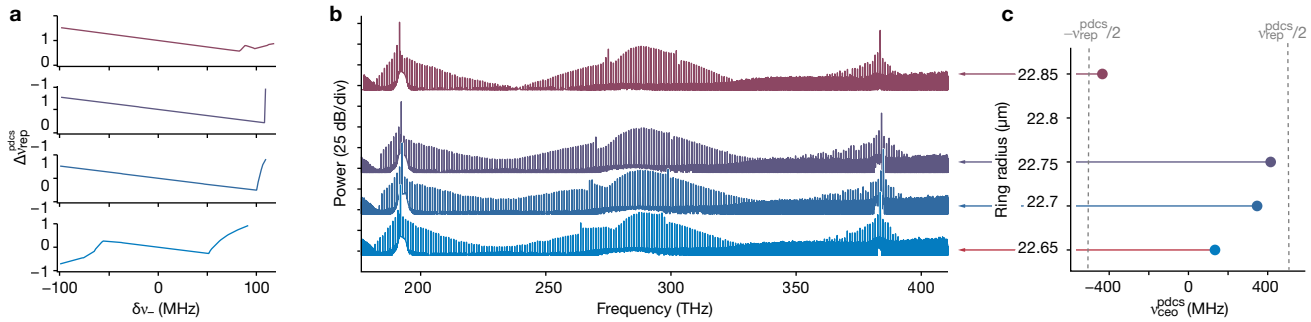


Fig. S.9 – Ring-radius engineering of the carrier-envelope offset frequency— Colors in **a** and **b** correspond to those in **c**, each identifying a given ring radius. **a** Repetition rate $\nu_{\mathrm{rep}}^{\mathrm{pdcs}}$ as a function of pump detuning $\delta\nu_{-}$ for self-aligned PDCSs generated in microrings with varying nominal ring radius, demonstrating self-alignment across all ring radii tested. **b** Optical spectra of the self-aligned PDCS for each ring radius, confirming that the octave-spanning single frequency grid is maintained across the 50 nm step ring radius variation. **c** CEO frequency $\nu_{\mathrm{ceo}}^{\mathrm{pdcs}}$ as a function of ring radius for the corresponding self-aligned states shown in **b**.

The CEO frequency of the self-aligned PDCS is bounded within $[-\nu_{\mathrm{rep}}^{\mathrm{pdcs}}/2, \nu_{\mathrm{rep}}^{\mathrm{pdcs}}/2]$ and can therefore be large, requiring frequency downconversion for direct detection. In standard DKS, ring radius engineering[17] tunes the CEO without altering the dispersion, and has been used to reach directly detectable $\nu_{\mathrm{ceo}}^{\mathrm{pdcs}}$.[18,19] The same approach can be applied in the case of self-aligned PDCS. To show this, we consider devices from the same wafer as Fig. 3 ($H = 680$ nm

Si_3N_4), with geometry parameters $RW = 860$ nm, $G = 450$ nm, $L_c = 17$ µm, and $W_g = 460$ nm. For ring radii ranging from 22.65 µm to 22.9 µm, each device generates a self-aligned PDCS at quasi-harmonic pump frequencies (Fig. S.9a,b), while ν_{ceo}^{pdcs} varies by approximately 100 GHz (Fig. S.9c) per device, covering almost the entirety of the CEO space. Additionally, this CEO change per 50 nm ring radius variation matches approximately that of the integrated heater tuning shown in Fig. 3d. Thus, if the electro-optic phase modulator for CEO downconversion is undesirable, ring radius engineering and thermal tuning together can shift the CEO toward zero, reaching a value directly detectable with off-the-shelf photodetectors.

S.9. Cross correlation measurement of the repetition rate

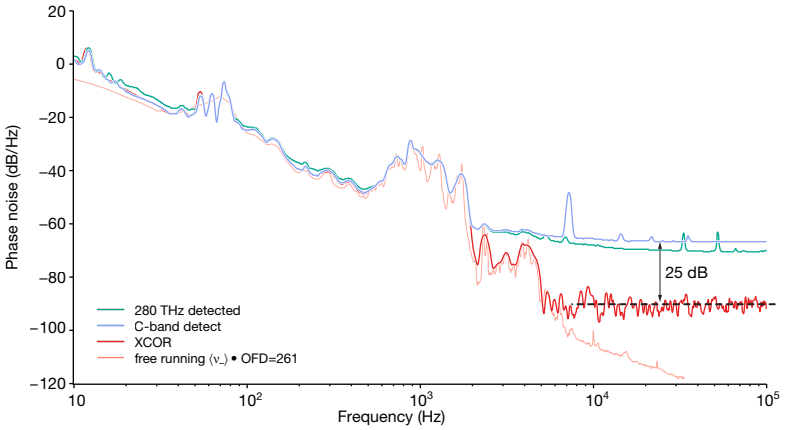


Fig. S.10 – Cross-correlation measurement of PDCS repetition rate— PDCS Repetition rate phase noise power spectral density with and without cross-correlation (XCOR). Here the positive pump locks the CEO and the negative pump runs freely; hence the repetition rate follows OFD of the latter's noise (pink). When frequency downconverting ν_{rep}^{pdcs} with an electro-optic phase modulator EO comb apparatus, its noise limits detection beyond 2 kHz. By measuring the repetition rate in both the C-band (blue) and at the center of the PDCS around 280 THz (teal) with independent EO combs, we perform an XCOR measurement where each EO comb downconverter acts as an input to the phase noise analyzer. This rejects the uncorrelated EO comb noise and lowers the noise floor by approximately 25 dB (red).

With the repetition rate of the PDCS ν_{rep}^{pdcs} being in the 730 GHz range, we cannot directly detect it through photodetection of two adjacent comb teeth. Instead, as discussed in the Methods, we use an electro-optic phase modulation apparatus, also known as an electro-optic comb (EO comb), that acts as a local oscillator to down-convert the PDCS repetition rate to a detectable frequency $\nu_{IF}^{rep} = \nu_{rep}^{pdcs} - m\nu_{rf}^{rep}$. Therefore, the phase noise power spectral density that we measure is such that $\langle \nu_{IF}^{rep} \rangle = \langle \nu_{rep}^{pdcs} \rangle + m\langle \nu_{rf}^{rep} \rangle$. Hence, as in any frequency down-conversion scheme, the local oscillator phase noise $m\langle \nu_{rf}^{rep} \rangle$ adds to the measured phase noise of the PDCS repetition rate. Although high-quality microwave sources are available, the multiplication factor m from the number of EO sidebands needed to span two adjacent PDCS teeth is large ($m \approx 42$ here). Therefore, this produces a high noise floor, particularly for Fourier frequencies above 2 kHz (Fig. S.10).

A method to overcome this EO comb noise floor limitation is to use the two input channels of the phase-noise analyzer (PNA) to perform a cross-correlation (XCOR) measurement. In such a scheme, the device under test (DUT) is measured in two independent ways, so that the uncorrelated noise from the two DUT inputs is rejected. Therefore, by frequency down-converting ν_{rep}^{pdcs} using two independent EO combs, their uncorrelated noise will be rejected, leaving only the PDCS repetition rate phase noise. We implement such a scheme using the large spectral span of the PDCS and measuring the repetition rate around 280 THz (*i.e.*, close to the PDCS center) and in the C-band, two modes away from the negative pump (see Fig. S.11). Using this technique, the phase noise PSD $\langle \nu_{IF}^{rep} \rangle$ from both EO comb detections shows the same profile, confirming the same repetition rate throughout the PDCS spectrum. Using these two as the DUT inputs of the PNA, we show a reduction of about 25 dB with respect to the single EO comb-limited noise floor, enabling more accurate measurement. The limitation in further noise floor reduction comes from the limited averaging available in the XCOR measurement. Indeed, the frequency drift, even when locked to the reference cavity (as seen in the Allan deviation in Fig. 4c), limits the total averaging time to about 5 min before the frequency drift prevents proper correlation between the two channels and better averaging. However, the currently observed reduction in the noise floor is sufficient to demonstrate the optical frequency division in all the locking regimes studied.

S.10. Complete experimental apparatus

The complete experimental apparatus used in this work is shown in Fig. S.11. In our self-aligned PDCS system, both pumps generate and trigger the synchronization of the cavity soliton, thereby becoming comb teeth. The independent locking of the two pumps on the input side enables stabilization *before PDCS generation*, except in the microwave-to-optical coherent link case, where self-stabilization requires that the detected repetition rate ν_{rep}^{pdcs} be fed back for locking.

Thus, we detect the heterodyne between the doubled negative pump ν_- and the positive pump ν_+ to lock what will become the CEO frequency ν_{ceo}^{pdcs} once the PDCS is generated (Fig. S.11, block ①). We note that since the

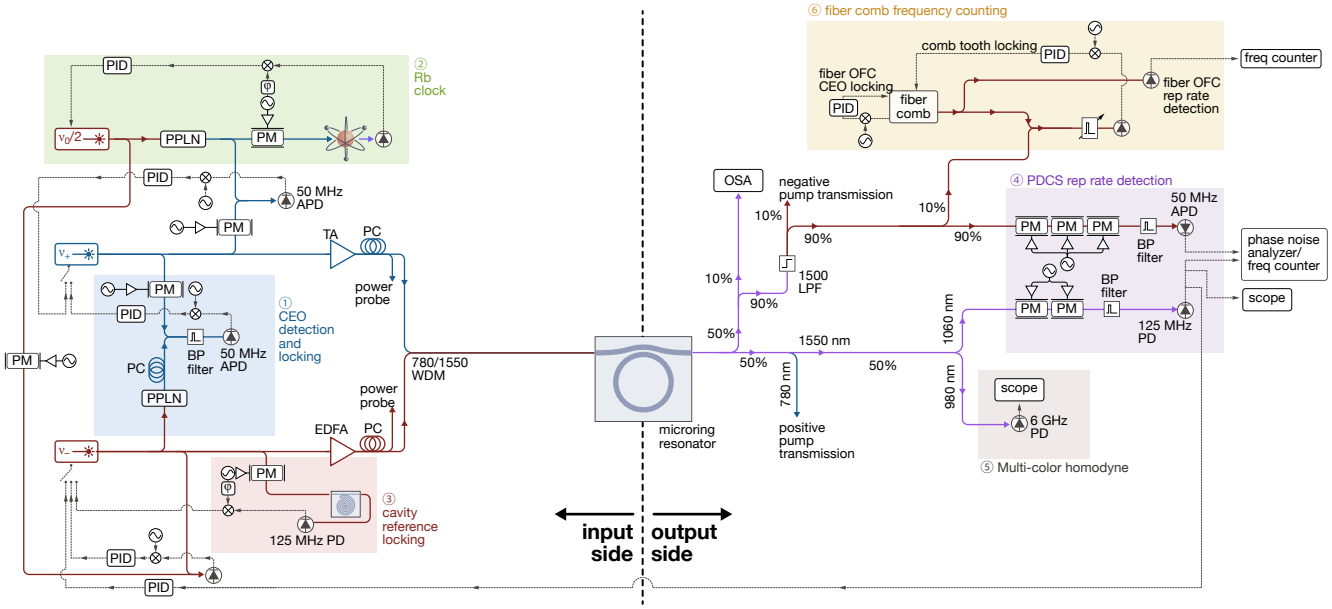


Fig. S.11 – Complete experimental setup—Complete experimental apparatus used to generate, self-align, and characterize the PDCS. The input side (left) is comprised of the two pump lasers ν_- and ν_+, amplified by a TA and an EDFA, respectively, that are sent into the microring resonator. Each laser is tapped for setting and stabilizing the CEO of the subsequently generated PDCS comb (blue block ①), locking the lasers to the Rb clock (green block ②), or locking the negative pump to the reference cavity (red block ③). The output side (right) is solely used to characterize the PDCS, with the exception of the self-stabilized microwave-to-optical link case, where the repetition rate detection (purple block ④) is fed back to the negative pump laser to lock it, and cannot be done otherwise. The fiber comb (yellow block ⑤) is used to measure the absolute frequency of the PDCS comb teeth. The multicolor homodyne to detect $\Delta\nu_{\mathrm{ceo}}$ is displayed in the gray block ⑥. PC: polarization controller; TA: tapered amplifier; EDFA: erbium-doped fiber amplifier; WDM: wavelength-division multiplexer; OSA: optical spectrum analyzer; PM: electro-optic phase modulator; LPF: long-pass filter; BPF: band-pass filter; PD: photodetector; APD: avalanche photodetector; PID: proportional-integral-derivative controller; PPLN: periodically-poled lithium niobate waveguide;

CEO detection occurs *before* the chip, the power available exceeds any on-chip light generated (either by the PDCS or any other DKS). Therefore, we do not require amplification of the negative pump laser while using a commercial fiber-pigtailed periodically poled lithium niobate (PPLN) crystal and still obtain a doubled power $P_{2\nu-} \approx 10$ µW, which we beat against a phase-modulated tap of the positive pump, at a power $P_{\nu+} \approx 1$ mW. As described in the Methods section, $\nu_{\mathrm{ceo}}^{\mathrm{pdcs}}$ lies beyond our detectable microwave range, and thus the phase-modulation of the tapped pump is done in the overdriven regime, resulting in an electro-optic comb for frequency downconversion. The frequency downconverted CEO $\nu_{\mathrm{IF}}^{\mathrm{ceo}}$ is then phase-locked to the 10 MHz microwave reference by feedback on one of the lasers, which in Fig. S.11 is the positive laser. Alternatively, the input laser can be locked to the Rb clock laser (Fig. S.11, block ②) where a CW laser is doubled and locked to the $5S_{1/2}$-$5D_{5/2}$ two-photon transition of the ^{87}Rb vapor, which is set in a 100 °C gas cell. The clock laser is phase (frequency) modulated and sent through the vapor cell, similar to a Pound-Drever-Hall (PDH) technique. The atoms are preferentially excited by resonant light, and fluoresce as they relax back to the $5S_{1/2}$ state. We detect the power of this fluorescence. We deliberately phase modulate the laser slower than the atomic relaxation rate in order to keep a good contrast on the detected signal. The difference from a standard PDH approach is that the power of the fluorescence (incoherent) is detected instead of the probe laser power, and that there are therefore no off-resonance sidebands for the signal to interfere with. From there it is the same control loop as a PDH, with lock-in and servo feedback. The fundamental and second harmonic of this laser are then used to lock the negative and positive pump lasers, respectively, using heterodyne detection and feedback on each laser current. Finally, the positive pump can be locked to a high-finesse reference cavity (Fig. S.11, block ③) using PDH locking.

The output of the experimental setup is dedicated to the characterization of the PDCS. A portion is extracted to probe the PDCS spectrum using an optical spectrum analyzer (OSA). Another portion is sent to the repetition rate detection block (Fig. S.11, block ④), using appropriate wavelength demultiplexers (WDMs) to select the desired spectral region for $\nu_{\mathrm{rep}}^{\mathrm{pdcs}}$ detection. EO combs at 1550 nm (190 THz) and 1060 nm (280 THz), consisting of two and three phase modulators respectively, down-convert the PDCS repetition rate to obtain two $\nu_{\mathrm{IF}}^{\mathrm{rep}}$ signals. In the case of self-stabilization for a microwave-to-optical link, the 1060 nm-detected $\nu_{\mathrm{IF}}^{\mathrm{rep}}$ provides feedback to the pump laser to lock the PDCS repetition rate to the 10 MHz reference. In the optical-to-microwave link case, the two detected $\nu_{\mathrm{IF}}^{\mathrm{rep}}$ are used for the XCOR measurement to reject the EO comb noise floor, as discussed in Section S.9. To characterize

the optical frequency of the PDCS comb teeth, a portion of the PDCS output is heterodyned against a fiber comb whose CEO is locked to the 10 MHz reference and whose repetition rate is locked to a given PDCS comb tooth. This configuration enables precise optical frequency counting from the optical frequency division operation of the fiber comb. Finally, a portion of the PDCS is extracted around 980 nm (*i.e.* 305 THz) to monitor the multi-color beat $\Delta\nu_{\mathrm{ceo}}$ between the PDCS and the pump comb components, which vanishes when the PDCS becomes self-aligned.

[1] H. Taheri, A. B. Matsko, and L. Maleki, Optical lattice trap for Kerr solitons, The European Physical Journal D **71**, 153 (2017).

[2] G. Moille, Z. Li, S. Shamailov, M. Leonhardt, D. Paligora, N. Englebert, F. Leo, J. Fatome, K. Srinivasan, and M. Erkintalo, Existence, stability, and characteristics of pure-Kerr parametrically driven cavity solitons, SPIE Photonics West **Laser Resonators, Microresonators, and Beam Control XXVII**, PC1334908 (2025).

[3] G. Moille, P. Shandilya, J. Stone, C. Menyuk, and K. Srinivasan, All-optical noise quenching of an integrated frequency comb, Optica **12**, 1020 (2025).

[4] C. R. Menyuk and S. Wang, Spectral methods for determining the stability and noise performance of passively modelocked lasers, Nanophotonics **5**, 332 (2016).

[5] Z. Qi, S. Wang, J. Jaramillo-Villegas, M. Qi, A. M. Weiner, G. D'Aguanno, T. F. Carruthers, and C. R. Menyuk, Dissipative cnoidal waves (Turing rolls) and the soliton limit in microring resonators, Optica **6**, 1220 (2019).

[6] S. Bai, Z. Tang, Z. Huang, and J. Yu, Thermal characterization of Si_3N_4 thin films using transient thermoreflectance technique, IEEE Transactions on Industrial Electronics **56**, 3238 (2009).

[7] R. Huszank, L. Csedreki, Z. Kertész, and Z. Török, Determination of the density of silicon–nitride thin films by ion-beam analytical techniques (RBS, PIXE, STIM), Journal of Radioanalytical and Nuclear Chemistry **307**, 341 (2016).

[8] T. E. Drake, J. R. Stone, T. C. Briles, and S. B. Papp, Thermal decoherence and laser cooling of Kerr microresonator solitons, Nature Photonics **14**, 480 (2020).

[9] J. M. Lukens, K. V. Myilswamy, A. Miloshevsky, and H.-H. Lu, Beyond critical coupling: Optimal design considerations for spontaneous four-wave mixing in microring resonators, Optics Express **34**, 2782 (2026).

[10] N. S. Tatarinova, A. E. Shitikov, G. V. Grechko, A. K. Vorobyev, A. V. Masalov, I. A. Bilenko, D. A. Chermoshentsev, and V. E. Lobanov, Optimization of the threshold for degenerate optical parametric oscillations in a bichromatically pumped microresonator, Physical Review Applied **24**, 024010 (2025).

[11] S. Zhang, J. M. Silver, L. Del Bino, F. Copie, M. T. M. Woodley, G. N. Ghalanos, A. Ø. Svela, N. Moroney, and P. Del'Haye, Sub-milliwatt-level microresonator solitons with extended access range using an auxiliary laser, Optica **6**, 206 (2019).

[12] H. Zhou, Y. Geng, W. Cui, S.-W. Huang, Q. Zhou, K. Qiu, and C. Wei Wong, Soliton bursts and deterministic dissipative Kerr soliton generation in auxiliary-assisted microcavities, Light: Science & Applications **8**, 50 (2019).

[13] N. Englebert, F. De Lucia, P. Parra-Rivas, C. M. Arabí, P.-J. Sazio, S.-P. Gorza, and F. Leo, Parametrically driven Kerr cavity solitons, Nature Photonics **15**, 857 (2021).

[14] G. Moille, M. Leonhardt, D. Paligora, N. Englebert, F. Leo, J. Fatome, K. Srinivasan, and M. Erkintalo, Parametrically driven pure-Kerr temporal solitons in a chip-integrated microcavity, Nature Photonics **18**, 617 (2024).

[15] G. Moille, Q. Li, T. C. Briles, S.-P. Yu, T. Drake, X. Lu, A. Rao, D. Westly, S. B. Papp, and K. Srinivasan, Broadband resonator-waveguide coupling for efficient extraction of octave-spanning microcombs, Optics Letters **44**, 4737 (2019).

[16] G. Moille, D. Westly, R. Shrestha, K. T. Hoang, and K. Srinivasan, Broadband Visible Wavelength Microcomb Generation In Silicon Nitride Microrings Through Air-Clad Dispersion Engineering, Laser & Photonics Reviews , 2401746 (2025).

[17] J. Zang, H. Liu, T. C. Briles, and S. B. Papp, Foundry manufacturing of octave-spanning microcombs, Optics Letters **49**, 5143 (2024).

[18] D. T. Spencer, T. Drake, T. C. Briles, J. Stone, L. C. Sinclair, C. Fredrick, Q. Li, D. Westly, B. R. Ilic, A. Bluestone, N. Volet, T. Komljenovic, L. Chang, S. H. Lee, D. Y. Oh, M.-G. Suh, K. Y. Yang, M. H. P. Pfeiffer, T. J. Kippenberg, E. Norberg, L. Theogarajan, K. Vahala, N. R. Newbury, K. Srinivasan, J. E. Bowers, S. A. Diddams, and S. B. Papp, An optical-frequency synthesizer using integrated photonics, Nature **557**, 81 (2018).

[19] Z. L. Newman, V. Maurice, T. Drake, J. R. Stone, T. C. Briles, D. T. Spencer, C. Fredrick, Q. Li, D. Westly, B. R. Ilic, B. Shen, M.-G. Suh, K. Y. Yang, C. Johnson, D. M. S. Johnson, L. Hollberg, K. J. Vahala, K. Srinivasan, S. A. Diddams, J. Kitching, S. B. Papp, and M. T. Hummon, Architecture for the photonic integration of an optical atomic clock, Optica **6**, 680 (2019)